A Study of Near Tip Phenomena for Cracks

in a Particulate Composite

by

Mohamad A. Rezvani

Dissertation submitted to the Faculty of the

Virginia Polytechnic Institute and State University

in partial fulfillment of the requirements for the degree of

Doctor of Philosophy

in

Engineering Mechanics

APPROVED:

C. W. Smith, Chairman

D. Post

L. Meirovitch

R. H. Plaut

R. Czarnek

April 1989

Blacksburg, Virginia

A Study of Near Tip Phenomena for Cracks

In a Particulate Composite

by

Mohamad A. Rezvani

C. W. Smith, Chairman

Engineering Mechanics

(ABSTRACT)

An experimental investigation using grids with a frequency of 125 lines/in. (5 lines/mm) was performed on inert propellant and pure binder at two different global head rates of 0.1 in./min (2.5 mm/min) and 1.0 in./min (25.4 mm/min). From the extracted data, displacements, strains, and dominant eigenvalue for displacement were calculated. An idealized model was used to explain the high strain zone ahead of inert propellant that caused severe blunting at the crack tip.

Using the available algorithms and three dimensional photoelasticity, the dominant stress singularity order values were calculated in a four point single edged cracked bend specimen with both straight front and thumbnailed cracks. The free surface values are the same as for the inert propellant and in good agreement with analytical values.

A boundary layer is observed in the singularity order which extends towards the mid-plane of the specimen. This region is about twenty percent of the distance from the free surface to mid-depth of the fractured body.

The slow and fast head rates alter the global behavior of the specimen as well as the density of the displacement and strain contours. However, the near tip mechanisms are not altered.

Acknowledgements

I would like to express my sincere appreciation and respect to my committee chairman, Prof. C. W. Smith, for his invaluable guidance, suggestions and assistance in conducting this investigation and throughout my graduate work. Furthermore, a sincere note of thanks is also extended to the other members of my advisory committee, Dr. D. Post, Dr. L. Meirovitch, Dr. R. H. Plaut, and Dr. R. Czarnek, for their counsel and guidance throughout this investigation.

This investigation was sponsored by The Air Force Astronautics Lab. under contract No. F04611-87-C-0057. The guidance of Dr. C. T. Liu and the help of Mr. C. W. Chang and Mr. J. Lee in this work is appreciated.

I am also grateful to my friends, , , and , for their encouragement and support during my graduate work.

Special appreciation goes to my parents, . I will be forever thankful for the love, encouragement, confidence, and financial support they provided throughout all phases of my education.

Special thanks is also extended to my wife, , for her support, sacrifice and all the help she provided throughout my studies and in the completion of this manuscript. You made possible this dissertation and this degree.

This dissertation is dedicated to my parents and my wife.

Table of Contents

List of Illustrations

List of Tables

1.0 Introduction

Fracture mechanics concepts started in early 1920 with a publication of Griffith [1]. He stated that a crack would grow to lower the energy of the system, i.e., the energy would be dissipated by creating new fracture surfaces. He did his analysis based on Inglis' [2] work for stored energy calculations. Later on, Orowan [3] did some investigation on the plastic zone ahead of the crack tips of cracked bodies for materials that experienced brittle failure. In the late forties, Irwin [4] related stored strain energy to energy used to create new surfaces as well as plastic deformation. In 1955, Orowan [5] showed that if plastic work was taken into account in Irwin's work, the brittle fracture in materials could be well defined.

In 1957, Irwin [6] proved the equivalency of this energy approach to a stress intensity approach according to which fracture occurs when a critical stress distribution, characteristic of the material, is reached. By 1959, the Griffith-Irwin concept of sharp crack mechanics had received a lot of attention and a need for further investigation both analytically and experimentally was felt.

It should be mentioned that all the above discussions were for two dimensional Linear Elastic Fracture Mechanics, LEFM, and basically apply to sharp cracks in brittle materials [7]. For brittle materials, the plastic zone ahead of the crack tip is confined to a very small region.

Consideration of a free surface effect began around 1969 when Sih and Hartranft [8,9] suggested the possible loss of the square root stress singularity for cracks intersecting the free surface. Since then, different analytical and experimental approaches have been accomplished to measure both the stress intensity factors and the stress singularity orders as one moves from the center line of a cracked body to traction free surfaces.

Among the investigators were Folias [10,11] and Benthen [12-14] who carried out intensive analysis in this area. Further work has been performed by Bazant [15,16], Swedlow [17], and Takakuda [18]. All of the above work leads to the conclusion that, in fact, the square root stress singularity does vary from the classical value of 0.5 as one approaches the free surface. Its dependency on Poisson's ratio and the angle that the crack border makes with the free surface has also been established. In the next chapter, the work of these authors will be covered in more detail.

In 1980, Smith and Epstein started an intensive experimental investigation to resolve some of the ambiguity in analytical work in cracked bodies, specifically the stress singularity variation through the thickness. The artificial straight front crack was studied and the stress singularity orders were found through the thickness [19-23]. In these analyses, a boundary layer is observed in the singularity order which extends towards the mid-plane of the specimen. This region is about twenty percent of the distance from the free surface to mid-depth of the fractured body.

The other investigations of Smith, after the author joined his group, were measurements of the singularity values around the border of the crack front in semi-elliptical cracks in large plates, through cracks that were naturally grown in four point single edge cracked bend specimens, and continuation of Epstein's work [24-29].

2.0 Literature Review and Problem Definition

2.1 *Introduction*

As briefly mentioned in the previous chapter, studies of the effect of cracks intersecting free surfaces on the dominant stress singularity order started in the late sixties. Later, the investigation shifted towards deriving algorithms and analytical methods for the three dimensional cases where a crack intersects a free surface of the material. The surface is traction free and a very complex three dimensional state of stress exists at the crack tip. The value of the stress singularity order near the free surface was desired. Furthermore, the question of whether loss of the LEFM stress singularity is only at the surface or varies over a transition zone, or boundary layer, was of interest.

This chapter reviews some of the works carried out both analytically and experimentally in this area. The last section briefly gives a definition of the problem at hand that motivated this research.

2.2 The Work of Sih

Hartranft and Sih [8] based a three dimensional analysis for state of stress about a crack tip on the two dimensional eigenfunction expansion of Williams [30]. Using cylindrical coordinates as shown in Fig. 2.1, they developed the state of stress about the crack tip.

They assumed the stress singularity value of 0.5 at the free surface as well as inside the body throughout their analysis. To verify this approach and analysis, Villarreal and Sih [31] ran a three dimensional stress freezing photoelasticity test and removed thin slices starting at the plate surface orthogonal to the crack border in the neighborhood of 0.25 mm and thicker, Fig. 2.2. The value of K_I dropped towards the free surface from its interior values. The authors mentioned that their analysis is not valid in the region close to the free surface (i.e., the boundary layer), and the possibility that the inverse square root singularity may not hold true in that layer including the free surface.

2.3 The Work of Bazant

In 1974, Bazant [15,16] approached the problem of measuring the stress singularity at the free surface by numerical analysis. He used spherical coordinates, (r,θ,ϕ), in a semi-infinite body, Fig. 2.3. Since he assumed a semi-infinite domain, he could use a separation of variables approach and defined the displacements as follows:

$$U_{ij} = \sum_{K=1}^{\infty} r^{\lambda_0^K} f_{ij}^K(\theta, \phi) \qquad i,j = r,\theta,\phi \qquad (2.1)$$

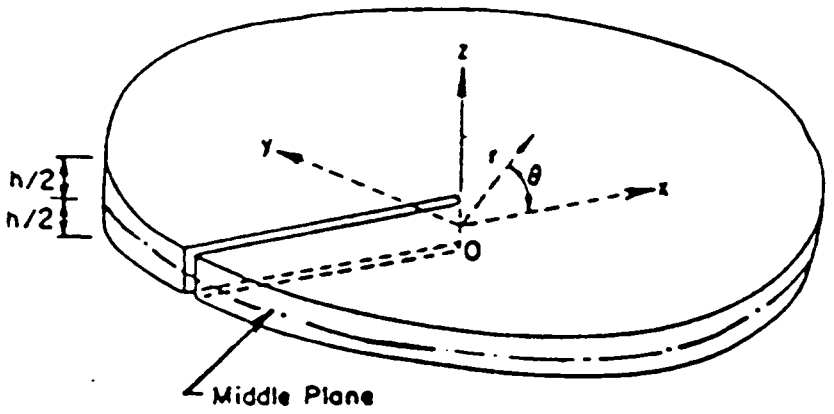

Figure 2.1. The geometry used by Sih [9].

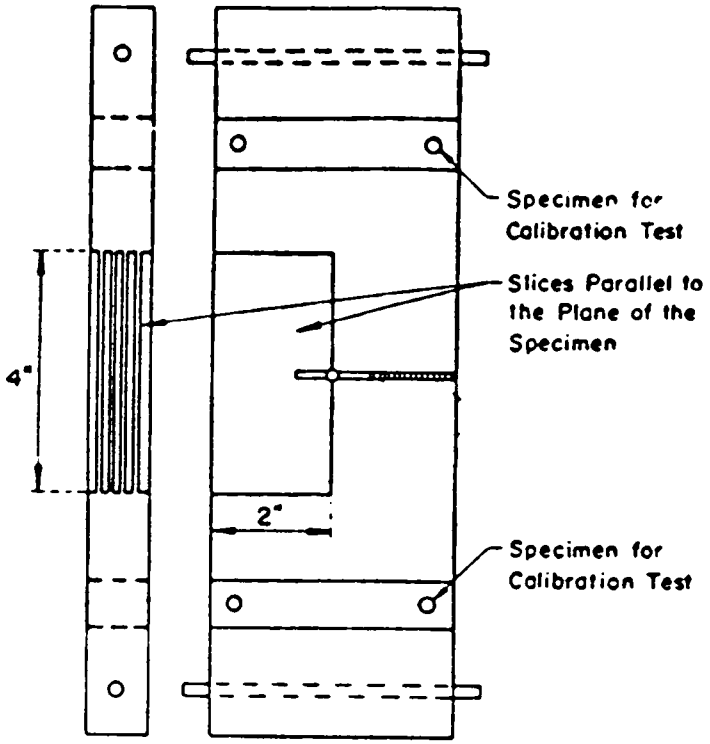

Figure 2.2. The geometry and slicing plane used by Villarreal and Sih [31].

He then substituted these equations into the spherical form of the Navier displacement equations. The displacements were a function of λ_u and he calculated a value of stress singularity ($|\lambda_\sigma| = 1 - |\lambda_u|$) of 0.329 for a Poisson's ratio of 0.25, for a stationary crack.

2.4 The Work of Folias

Folias [10] assumed a through crack in a finite width plate for his analytical work. He assumed the plate to be in tension in the direction perpendicular to the crack plane, Fig. 2.4. In his analysis he converted the three coupled partial differential equations of stresses with three independent variables to a system of three ordinary differential equations. He then wrote the displacements in terms of semi-infinite integrals with infinite series within the integrand. Furthurmore, he assumed the singular part of the solution to be a function of the leading term only. He finally found that the stress singularity is dependent on Poisson's ratio, (ν), in the form shown below:

$$r^{\lambda\sigma} = r^{-(\frac{1}{2}+2\nu)} \tag{2.2}$$

The work of Folias was not in good agreement with the work of the other analysts. The main question was whether his equilibrium conditions were satisfied with the stress series. In a paper published in 1980, [11], Folias tried to clarify some of the ambiguity by stating that "Due to mathematical intractability of solving certain integral equations, an unknown function exists in the singular term of the equation for the stress normal to the free surface". He states that "It is possible for this function to vanish at the free surface, thereby allowing the singularity to exist at the free surface," [32].

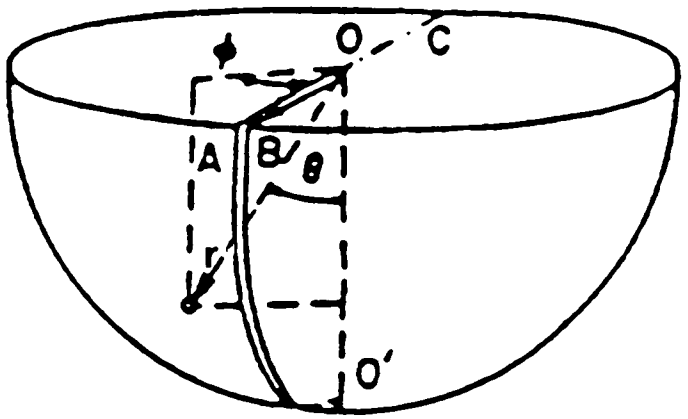

Figure 2.3. The geometry used by Bazant [16].

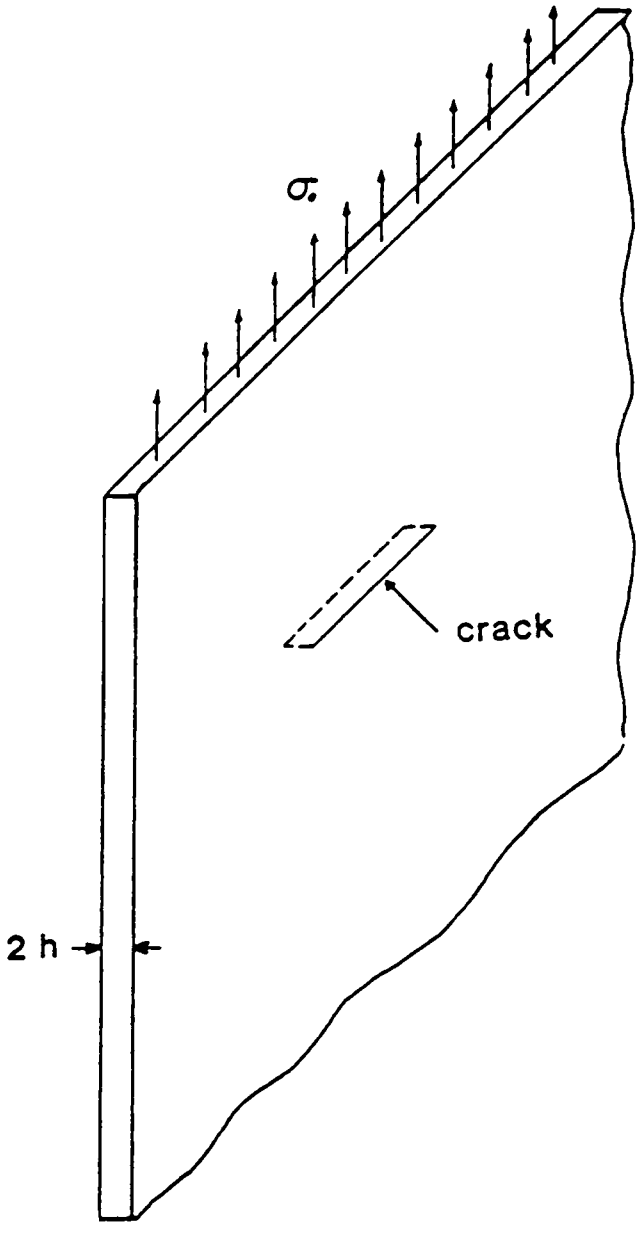

Figure 2.4. The geometry used by Folias [10].

2.5 The Work of Benthem

Benthem [13,14,33,34] in 1976 started the three dimensional analysis for stress and displacement eigenvalue measurements, and in the following years completed his studies. He also performed an experimental test. A review of his work is as follows:

Benthem used spherical coordinates as shown in Fig. 2.5 and a quarter infinite crack in a half space [33]. For displacement and stress fields, he used variable separable eigenfunction formulations. He took advantage of Neuber-Papkovitch-Bossinesq stress functions as a solution of the Navier-Cauchy equation. He defined stresses as follows:

$$\sigma_{ij} = \sum_{K=1}^{\infty} r^{\lambda\sigma^K} f_{ij}^{K}(\lambda_\sigma, \theta, \phi) \tag{2.3}$$

In his work he noted that the inverse square root singularity is lost at the free surface. This means the two dimensional analyses based on plane strain, as well as K_I, are invalid and meaningless at the free surface. He then calculated a different value of stress singularity at the free surface from the classical value of 0.5. He later did an experiment on rubber with $\nu = 0.5$, loaded in mode I, and found the singularity value at the free surface that agreed with his analysis. He also showed the dependency of the singularity order at the free surface on ν and Fig. 2.6 shows a plot of this relationship. It should be mentioned that the greatest difference in stress singularity from a value of 0.5 occurs (for real materials) when Poisson's ratio is one half.

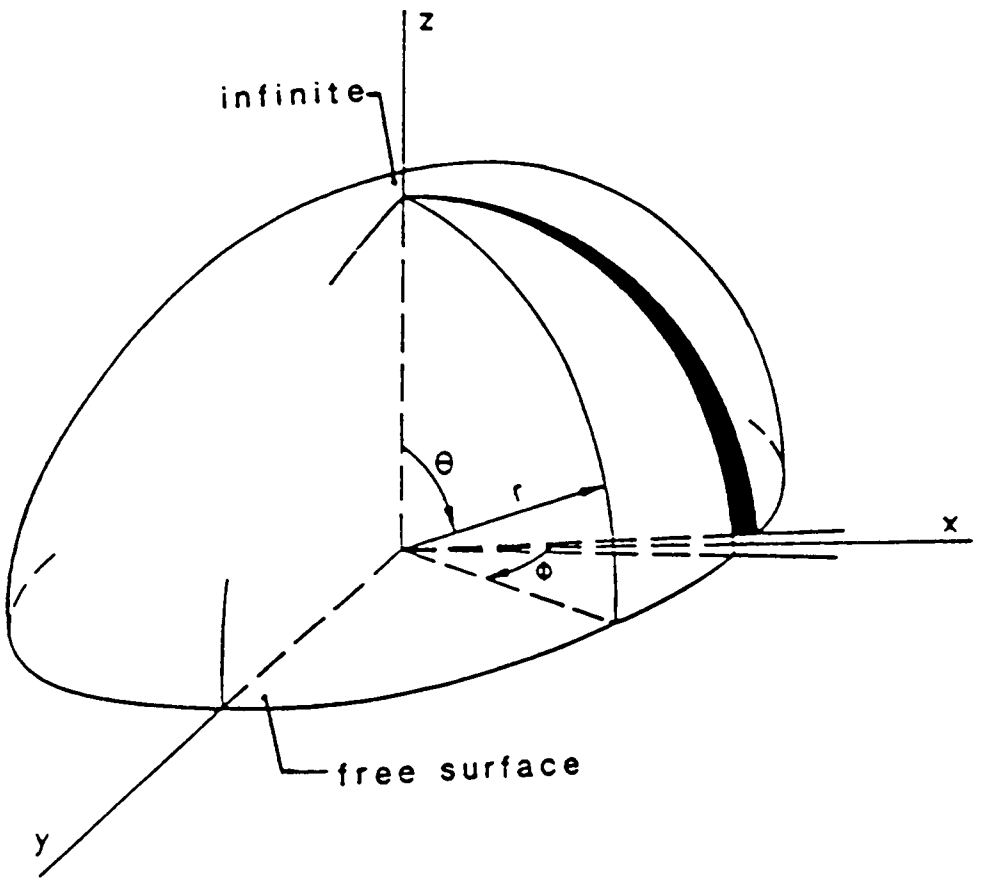

Figure 2.5. The geometry used by Benthem [33].

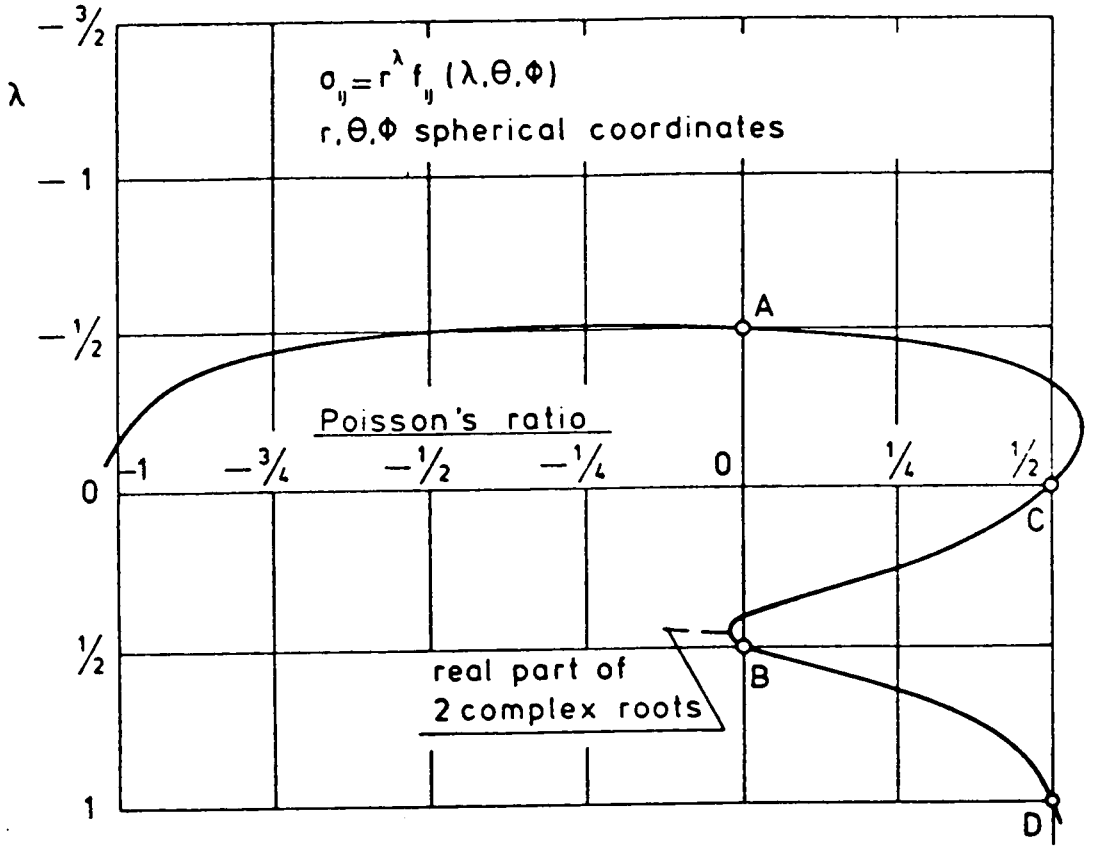

Figure 2.6. A plot of Benthem's first stress eigenvalue [33].

2.6 The Work of Kawai and Fujitani

Kawai and Fujitani [35,36] treated the problem by also using spherical coordinates and assuming a separation of variables approach. They formulated the stress function by using Bossinesq functions and Legendre polynomials. Collocation was used on the traction free surface for measurements of λ_σ. With a large number of collocation points, they approached the value of Benthem's at the free surface.

As the number of collocation points was reduced, the singularity value got closer to Folias' value [10,11]. This could imply that Folias' analysis was incomplete rather than incorrect.

2.7 The Work of Swedlow and Associates

In 1978, Swedlow published a paper, [17], where he addressed the problem of singularity computations. He attacked the problem by applying the finite element method. He used Williams' [30] approach for his analysis, and a number of finite element sections surrounding the singularity region for his formulations.

In 1984, Swedlow, with Burton and others, published another paper in which they combined the finite element method with boundary integral equations to measure the singularity order [37]. By application of boundary integral equations, all the field equations were exactly satisfied. Figures 2.7 and 2.8 show the geometries used by Swedlow and associates.

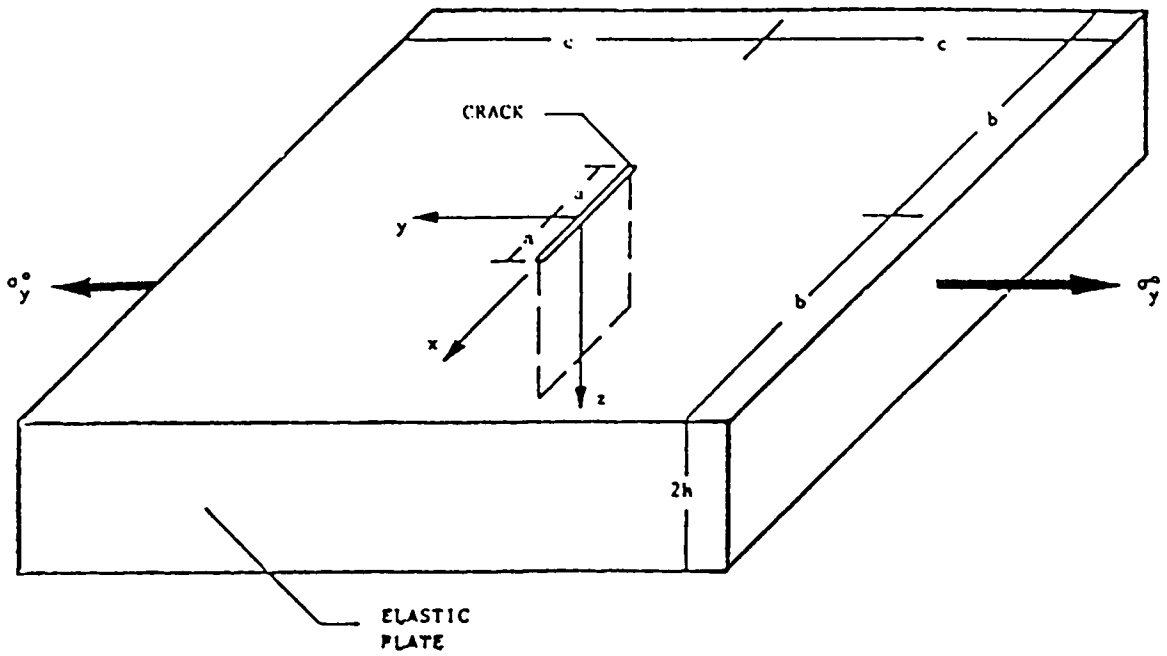

Figure 2.7. The geometry used by Swedlow for finite element formulation [37].

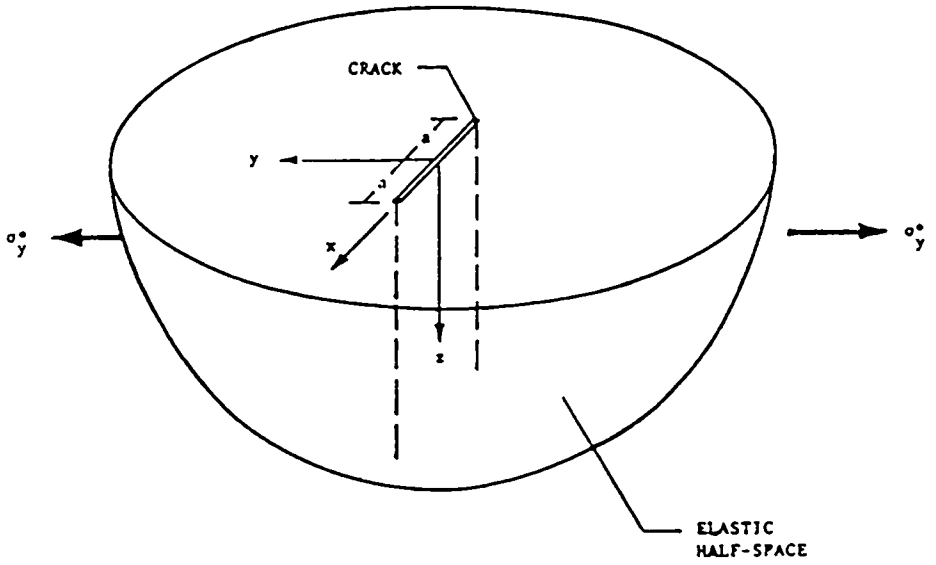

Figure 2.8. The geometry used by Swedlow for boundary integral formulation [37].

Swedlow's singularity values were in good agreement with those of the other researchers such as Benthem, Kawai, and Bazant, especially at lower values of Poisson's ratio. Table 2.1 shows the values and the respective sources [37].

2.8 The Work of Takakuda

Takakuda in 1985 published a paper in which he calculated the dominant eigenvalue for displacement for cracks intersecting the free surface [18]. The geometry he used for surface cracks is shown in Fig. 2.9. He formulated the crack problem in the form of integral equations and used Williams' approach for the Griffith crack under plane strain conditions to confirm his approach [30].

He considered the angle that a crack border would make with the free surface as a variable and took that into consideration for his analysis as well. Table 2.2 shows the values of the dominant eigenvalue for displacement that he calculated and listed with considerations of Poisson's ratio and the angle of the crack border with the free surface. His analysis showed that this angle would influence the dominant eigenvalue as much as Poisson's ratio does. For cracks intersecting the free surface at 90°, his value is very close to Benthem's value.

2.9 The Work of Smith, et al.

Smith, et al. started with approaching the measurement of stress singularity values from an experimental point of view [19-29]. Stress freezing photoelasticity, as will be described in more

Table 2.1. **The list of some stress singularity values at the free surface.**

Source	$\nu = 0.00$	$\nu = 0.15$	$\nu = 0.30$	$\nu = 0.40$
Analytical by Benthem	.500	.484	.452	.413
Analytical by Kawai	.500	.480	.430	.370
Finite difference by Benthem	.500	.484	.452	.414
FEM by Bazant	.500	.484	.452	.413
FEM by present method	.499	.485	.445	.370

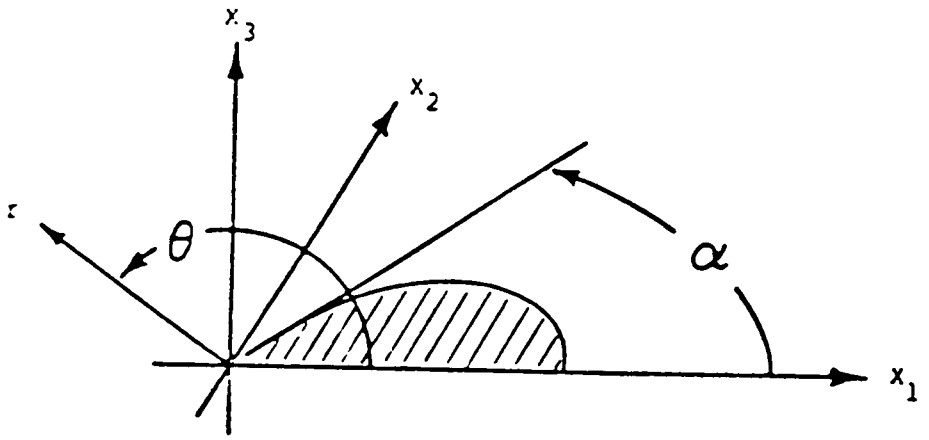

Figure 2.9. The geometry used by Takakuda [18].

Table 2.2. Takakuda's dominant eigenvalue for displacement at the free surface

α/π	$\nu=0.0$	$\nu=0.1$	$\nu=0.2$	$\nu=0.3$	$\nu=0.4$	$\nu=0.5$
0.125	0.8675	0.8861	0.9087	0.9354	0.9661	------
0.250	0.6944	0.7148	0.7464	0.7942	0.8687	------
0.375	0.5805	0.5946	0.6186	0.6578	0.7273	0.9493
0.500	0.4998	0.5096	0.5245	0.5477	0.5867	0.6684
0.625	0.4345	0.4403	0.4464	0.4540	0.4656	0.4864
0.750	0.3925	0.3888	0.3826	0.3740	0.3636	0.3527
0.875	0.3831	0.3706	0.3518	0.3283	0.3031	0.2789

detail in the following chapters, was used as a tool for this investigation. The motivation was that there was not a well established experimental procedure that would confirm the analytical and numerical work that had been carried out. The other concern of Smith was the value of the singularity within a transition zone towards the center line of the body. Physically he expected to have a transition zone, or boundary layer, as one moves from the free surface to the center line of the specimen. Smith's work started with measurements of the stress singularity through the thickness for a four point single edge cracked bend specimen with an artificial sharp through crack at the center [38]. The specimen geometry is shown in Fig. 2.10, with the lowest eigenvalue for displacement distribution in Fig. 2.11. To verify the values measured using a stress freezing process, moire interferometry was also applied.

The other work of Smith has been on measurements of the dominant stress singularity values for semi-elliptical natural cracks in finite thickness plates. This work was carried out after the author joined Smith [32]. The test model is shown in Fig. 2.12 and stress singularity values are shown in Fig. 2.13.

There have been some modifications to Epstein's analysis as well as more experimental work for a natural through edge crack in four point bend specimens that the author was involved in [24-27]. Additional studies for more complex geometries are planned and the values of the dominant stress singularity order will be extracted in the near future.

2.10 Problem Definition

This work basically is composed of two phases. First, there is a continuation of the research that has been going on by Smith and associates to get a better understanding of the three dimensional stress singularity values. The singularity values for an artificial sharp crack

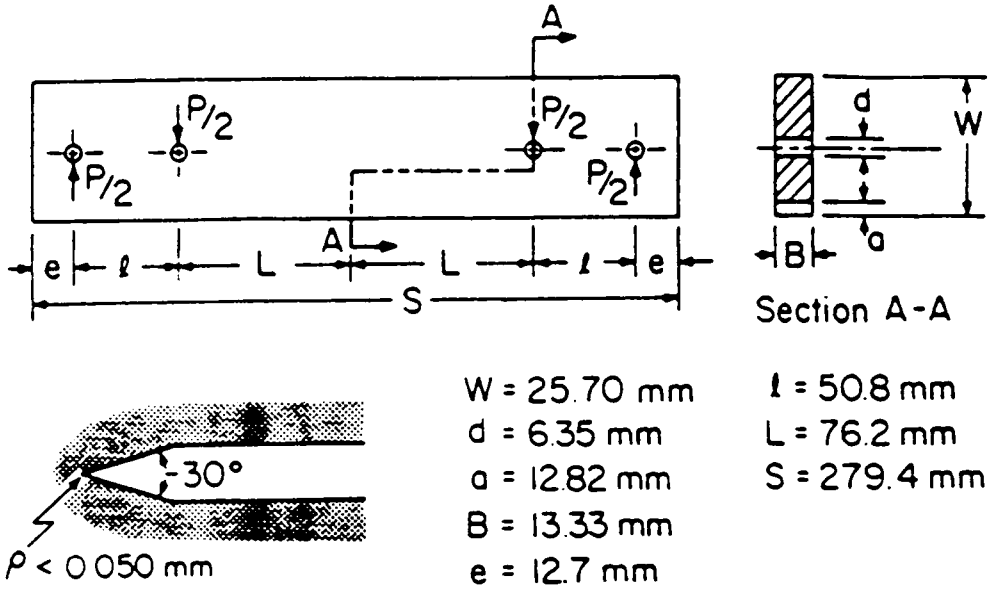

Figure 2.10. The specimen geometry used by Epstein [38].

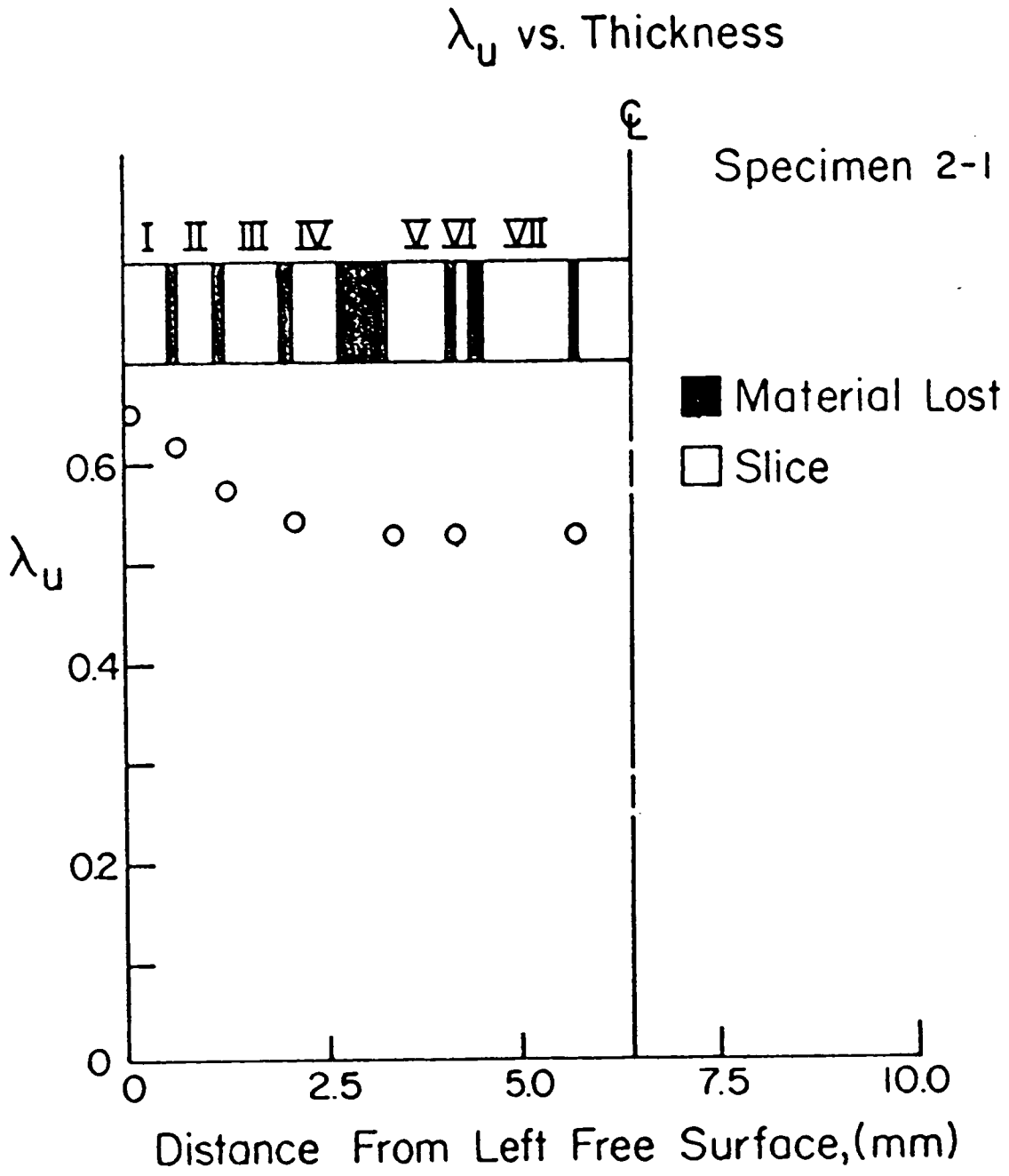

Figure 2.11. Epstein's dominant eigenvalue for displacement [38].

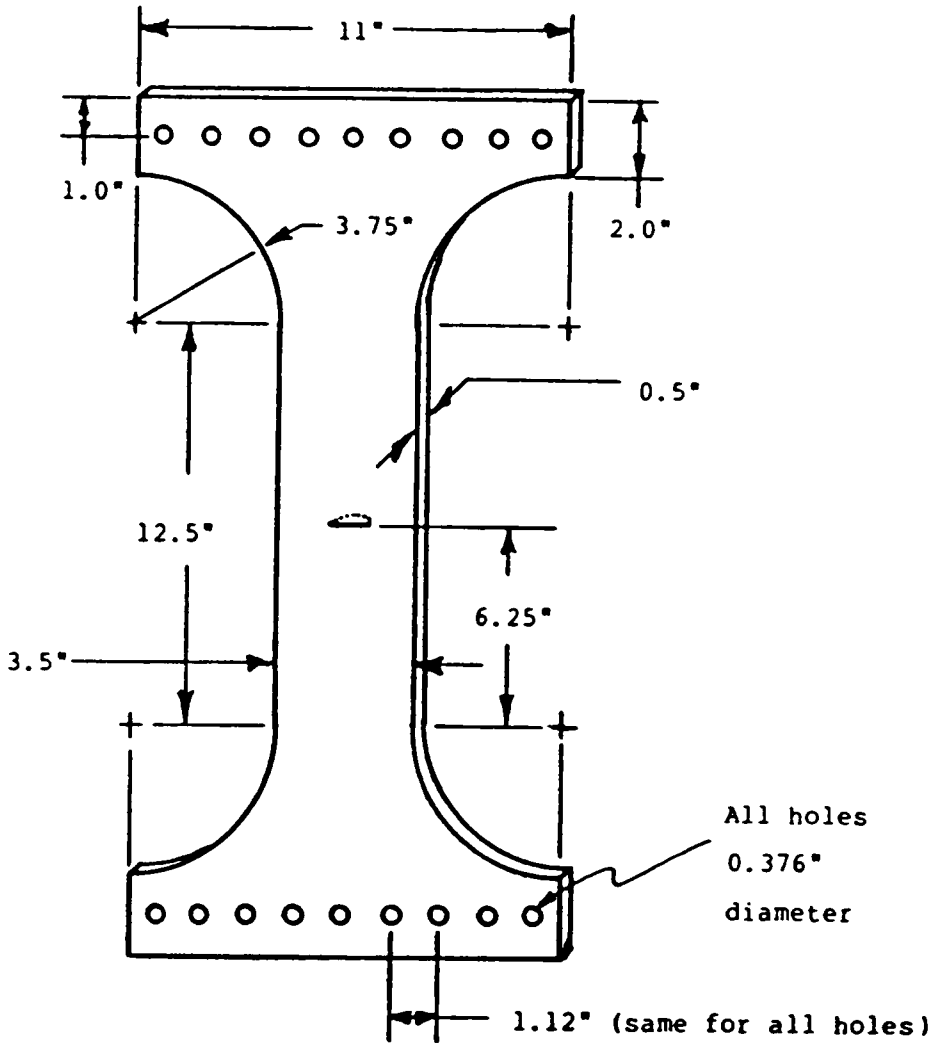

Figure 2.12. The specimen geometry used by Lloyd [32].

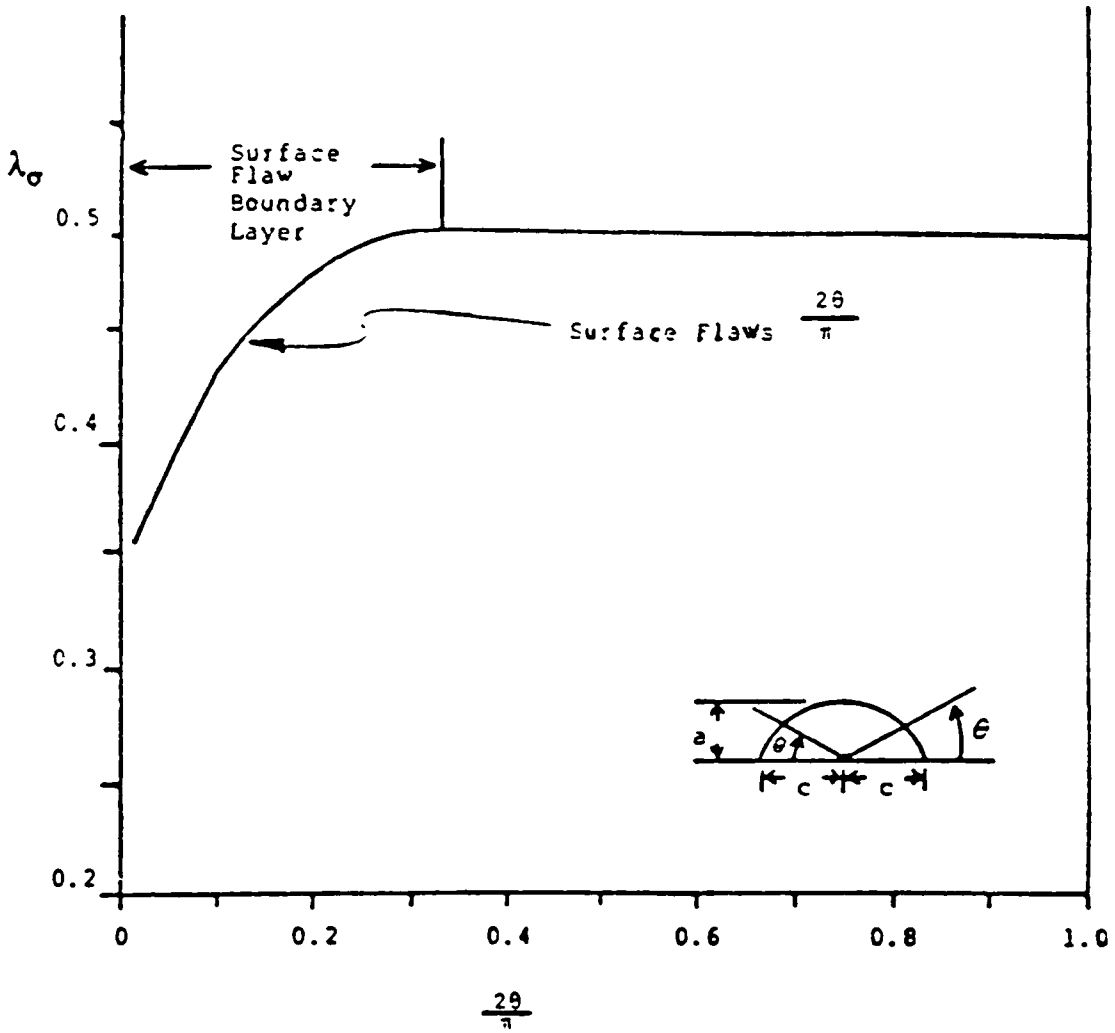

Figure 2.13. The stress singularity variation of Lloyd [32].

through the thickness of the specimen was calculated by the use of stress freezing material to benchmark the work of Epstein. The stress singularity values for a natural crack were also investigated. In this case, the same geometry as Epstein's work was used, except the crack was initiated with a sharp blade and grown naturally in the oven.

The second phase was an attempt to try to extend the above noted continuum approach to a particulate composite (i.e., solid fuel propellant). Solid fuel propellant consists of rigid particles in a rubbery matrix material. The material in general is non-homogeneous. The mechanical properties of the material have to be experimentally determined. The ingredients are chosen so as to maximize burning properties, but these properties are to some extent altered due to cracks developed in the motor grain. The cracks could develop in manufacturing or fabrication processes. In addition, some cracks could develop when the material is stored after being placed in its casing. The thermal expansion coefficients for the solid propellant and the casing are not the same, so variation of temperature in the storage area could create new cracks. Imperfect bonding between propellant and casing has also been observed, which could be idealized as a crack.

The cracks will reduce the strength of the material to some extent, but up to some point the reduced values may still be acceptable. One can use fracture mechanics to investigate these cracks and their effects on the behavior of the propellant. In this study, the values of in-plane displacements and strains at the surface of the propellant were desired. The matrix material of propellant, referred to as binder, has a volume of about 25% of the propellant and is a high Poisson ratio material. There was also interest in measuring the dominant eigenvalue for displacement in the propellant and binder at the free surface. Also, the shape of the crack border was to be investigated in the propellant and the stress freezing material. Finally, it was desired to determine to what extent the boundary layer and variation of the stress singularity measured in stress freezing material can be used to infer similar information about the propellant.

3.0 Experimental Procedures

3.1 Introduction

In this chapter the experimental procedures will be covered. It starts with a list and a short definition of the materials used. The different geometries as well as the experimental methods will also be discussed. The methods of data extraction are covered as well, so at the end of the chapter all required data would be available for analysis. The next chapter will concentrate on the analytical aspects of this dissertation. The experimental data read and collected here will be used as input for the next chapter.

3.2 Materials

Three types of materials were used through the course of this project. They are listed below and a brief definition of each will follow.

1. Inert Propellant
2. Pure Binder
3. PSM-9

3.2.1 Inert Propellant

This specimen material was manufactured by Morton Thiokol, Inc., and referred to as H-24 inert propellant. The word inert refers to the fact that the basic ingredients of a real propellant were kept in this material, except that burning particles were replaced by other crystals. The result is a non-homogeneous composite of very stiff inclusions in a compliant matrix of polybutadiene resin. The volume fraction of inclusions is approximately 75%. The output is a rubbery gray solid with ingredients listed below [39]:

Polybutadiene Resin	10% by wt.
Potassium Chloride	70% by wt.
Powdered Aluminum	15% by wt.
Ammonium Perchlorate	5% by wt.

The manufacturer's specifications indicated that the maximum size of particles would be 0.008 in. (200 μm). Looking at the material under a microscope revealed particles as large as 0.020 in. (500 μm). It was also specified that properties of the material would change upon exposure to moisture. During storage the material was kept in sealed bags except when being tested.

3.2.2 Pure Binder

Pure binder was classified as a homogenous material made by casting the polybutadiene resin that was used in the propellant. It had a Poisson's ratio of about 0.47 and Young's modulus of 112.3 psi (0.776 Mpa) at room temperature at nominal global strains of up to 20%.

Some chemical additives, used to enhance the capability of bonding the rubber to propellant particles, were also added to the binder. The result was a very soft light yellow colored rubber. Pure binder was also manufactured by Morton Thiokol, Inc., and referred to as R54M Gumstock.

3.2.3 PSM-9

This material was used for the stress freezing process. It was an epoxy cast in sheets of different thicknesses and the specimens were made out of these sheets. It had diphase mechanical and optical properties, one set at room temperature and one set above its critical temperature of about 220 °F (105 °C). At room temperature, it had a stress-optic coefficient, f, of 60 psi/fringe/in. (10.5 Kpa/fringe/m) with Young's modulus of 480 Ksi (3.3 Gpa). At elevated temperature, critical temperature, the value of f was reduced to 2.5 psi/fringe/in. (438 pa/fringe/m), and Young's modulus dropped to 6000 psi (0.04 Gpa).

The Poisson's ratio of 0.36 at room temperature reached the value of incompressible elastic materials (0.50) at critical temperature with no viscoelastic effects [40]. The pure binder was also nearly incompressible at room temperature.

Since PSM-9 (referred to as stress freezing material here as well) is cast in sheets. For each new sheet a calibration test was run to measure the actual Poisson's ratio, fringe constant, and Young's modulus.

3.3 Grid Method

The in-plane displacements and strains as well as the lowest displacement eigenvalue for the free surface of pure binder and inert propellant were desired around the crack tip. Since these materials were soft, large displacements and rotations were expected near the vicinity of the crack. A method of measurement that would yield reasonable results was needed. Of all the choices available, the grid method [41] seemed to fit this purpose the best. The method of applying the grid to the specimens is as follows [42]:

The region of interest, usually an area of 3x3 inches (7.5x7.5 cm) around the crack tip, was covered with a thin white coating of a mixture of silicone grease and Titanium dioxide powder. The excess material was wiped off carefully using "kimwipes". Then, under a microscope, a grid made of Nickel with 125 lines/in. (5 lines/mm) density was placed on the treated surface. Care was taken in lining up the grid lines with the line of the crack to ensure the accuracy of the displacement readings. Then the grid was pressed down on the specimen. Next, the specimen with attached grid was placed in a vacuum machine and a thin layer of Aluminum evaporated on it. The Aluminum turned black through the evaporation process. Removal of the mesh resulted in black Aluminum on openings of the grid, while the lines were left white.

The grids did not stiffen the free surface of pure binder or inert propellant. This was a major concern because both materials were very soft.

After the transfer process was completed, the area was photographed as shown in Fig. 3.1. The grid frequency was fine enough to show the displacements accurately, and at the same

time was coarse enough to be photographed clearly using a 35mm camera with extension tubes. This initial photograph, referred to as "initial pattern", acted as a master grating in geometric moire. Then specimens were loaded and deformed. The attached grid followed the specimen deformation and pictures were taken of the deformed stage at different global strain levels during constant displacement rate tests. In geometric moire, the contours of constant displacements would be obtained by superposition of the two pictures.

The process of superposition of the two images was bypassed by using a digitizing tablet and software developed in the lab. By fixing the picture to the digitizing tablet, the position of any grid could be recorded with respect to the crack tip. Then the same grid was traced and digitized in the deformed picture and recorded. The difference of the two yields the values of displacements at that specific grid.

Figure 3.2 shows a digitized area from one of the pictures. The digitized points are located at intersections of horizontal and vertical lines. Figure 3.3 shows the same points after the specimen has been loaded and deformed.

3.4 *Stress Freezing Photoelasticity Method*

The stress freezing process was used as a tool to measure the in-plane shear stresses and appropriate algorithms were used to convert them to fracture parameters [43]. The material used was PSM-9, a transparent plastic, with diphase mechanical and optical properties.

After the preparation of the specimen, it was placed in the oven and heated to critical temperature. Then it was soaked for a few hours at that temperature to avoid any temperature gradients. If an artificial crack was inserted in the specimen, some load would be applied and

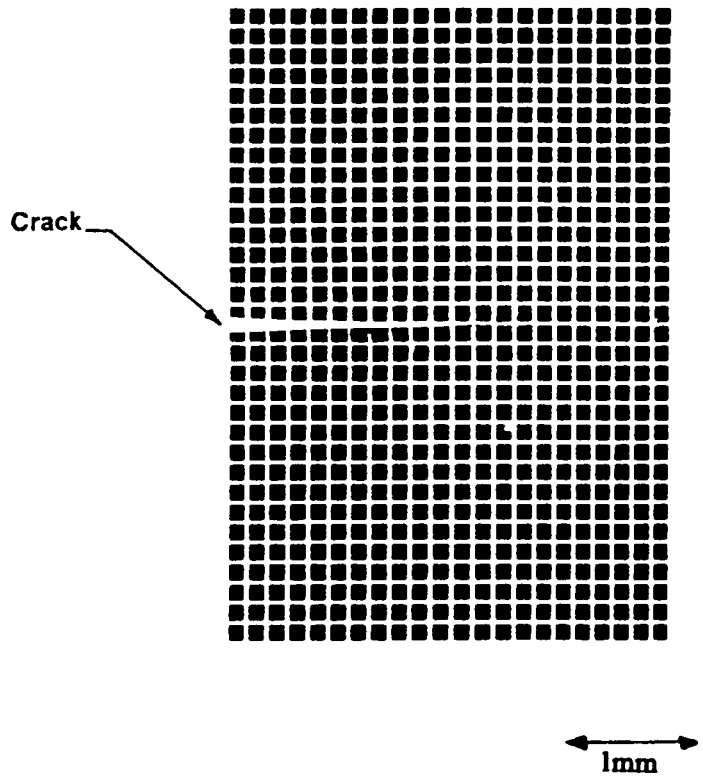

Figure 3.1. A picture of grid transferred to the surface of pure binder.

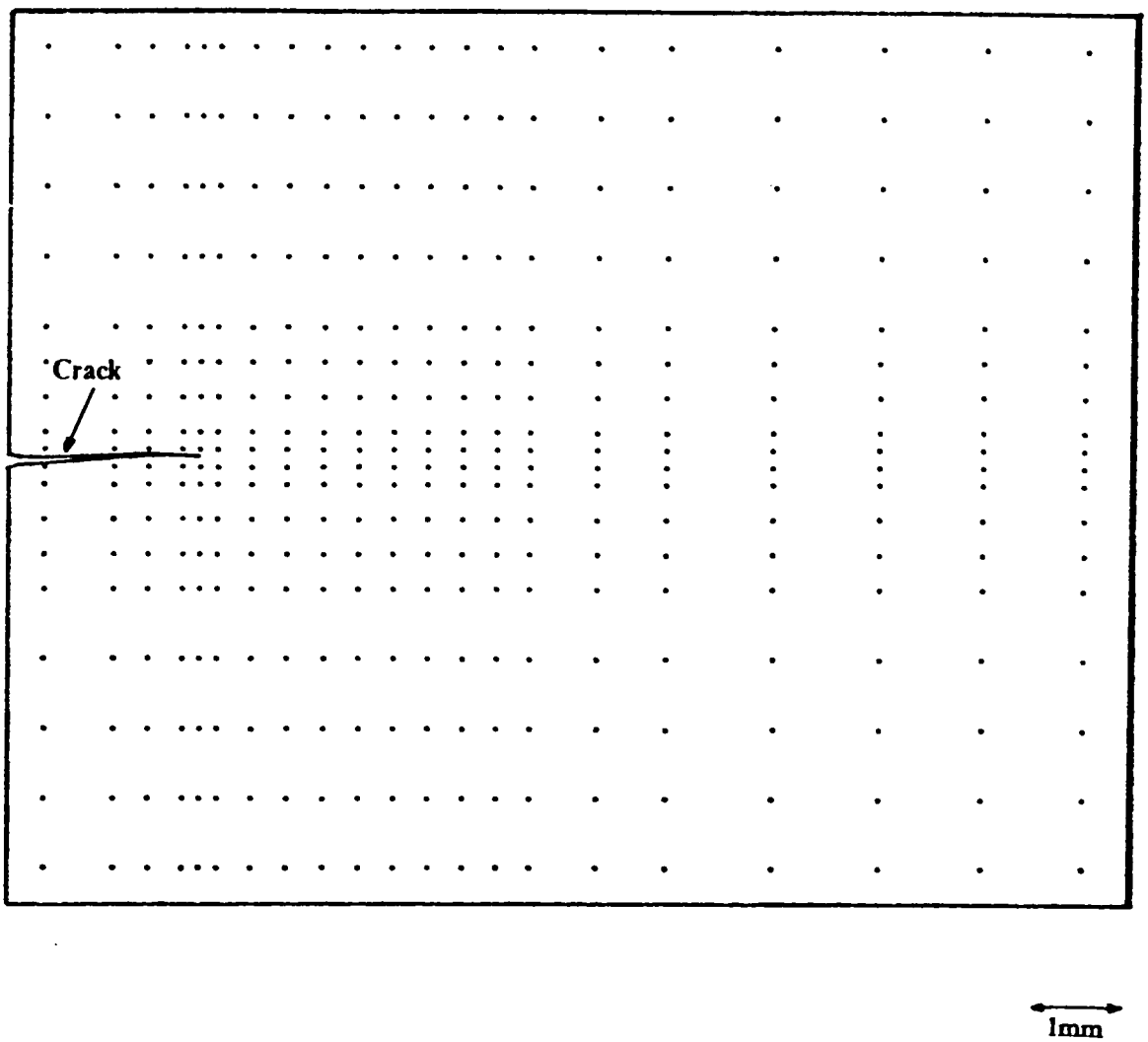

Figure 3.2. A digitized grid pattern before loading.

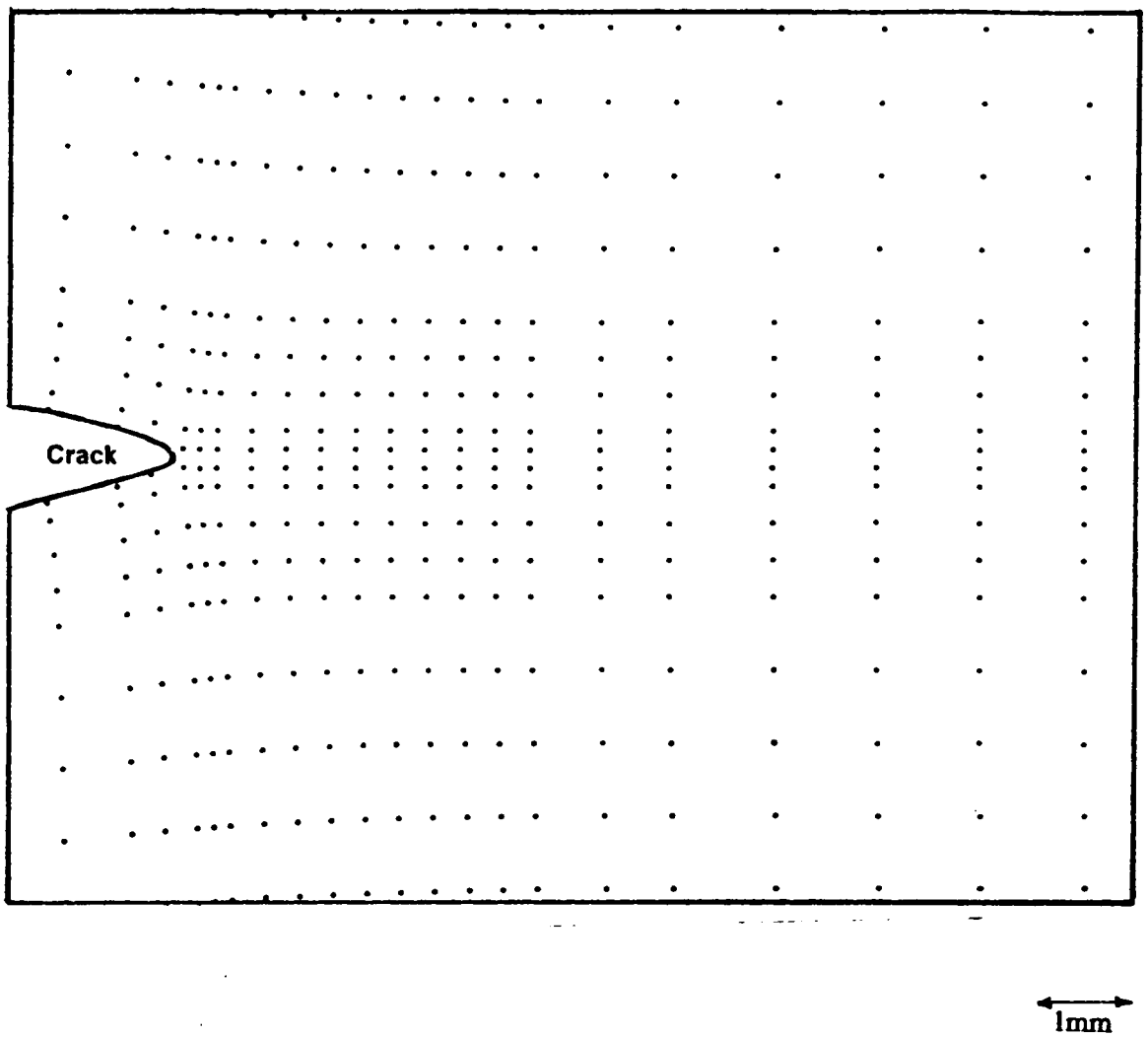

Figure 3.3. A digitized grid pattern after loading.

then the specimen was cooled to room temperature under load. On the other hand, if a natural crack was desired, the load would be monotonically applied to grow the crack. After the growth of the crack to the desired length, part of the load was reduced to arrest the crack growth. Then the specimen was brought to room temperature. The cooling process took a long time, because the specimen had to be cooled at a very slow rate. Upon cooling, all deformation would be frozen in the specimen. Removal of the load at room temperature resulted in negligible recovery. Then, using a Buehler diamond saw, slices were removed mutually orthogonal to the crack border and crack surface.

Keeping in mind the direct proportionality between stress fringe density and thickness of the slices, as will be covered in more detail in the next chapter, the Tardy compensation and the Post fringe multiplication methods were used to give fractional fringes. The result was increasing the number of data points.The Tardy compensation method was introduced by Tardy in 1929 [44]. Dally and Riley [45] cover this method in some detail and it will not be repeated here.

The Post fringe multiplication unit was set up by Epstein [38,46] and it effectively increased the thickness of the slice under consideration. These two processes, when combined, increased the number of fringes by more than one order of magnitude. Normally a fifth multiplication factor of fringes was used along with 18° ($\frac{\pi}{10}$rad) Tardy rotation for this purpose. Thus, the fringes as low as one fiftieth of a fringe order were recorded.

The fringe multiplication unit will be briefly explained here.

3.4.1 Fringe Multiplication Unit

As was mentioned earlier, when the stress freezing photoelastic process is used, one would get the stress fringes that are an indication of maximum in-plane shear stress applied to that

specimen. This maximum in-plane shear stress is directly proportional to the thickness of the material.

Upon removing the thin slices, the number of fringes would decrease, which in turn reduces the number of data points available for analysis. The fringe multiplication process increases the effective thickness of the slice, thus increasing the number of stress fringes. This idea was well defined in two papers by Post [47,48] and the set up was done by Epstein [38,46] and is shown in Fig. 3.4. Figure 3.5 shows a blow up of the fixture used in the field of the polariscope. The function of the multiplier unit is as follows:

A laser beam is collimated and reflected through a polariscope with a pair of partial mirrors in between. Then it passes through a focusing lens. The desired multiplication is chosen and a card with a thin slot blocks all the other beams except the chosen multiplication. Then it is reflected from a mirror to a ground glass viewing screen. The reading could be done using the stage or a picture could be taken and digitized.

Figure 3.5 shows the fixture. It has two partial mirrors which are set at some small angle with respect to each other, with a container that is filled with index matching fluid. The slice would be submerged in the fluid. As the light reaches the first partial mirror, part of it would reflect and part would go through the mirror. Then the light passes through the slice and to the second partial mirror. Again part of it goes through the second mirror, resulting in a multiplication of one, and part would reflect back. This process would continue and one can see the multiplications of one, three, five, seven and so on reaching the focusing lens. Figure 3.6 gives a graphical view of the explanation given above. Figure 3.7 shows fringe patterns for multiplications of one, five, and seventeen, respectively.

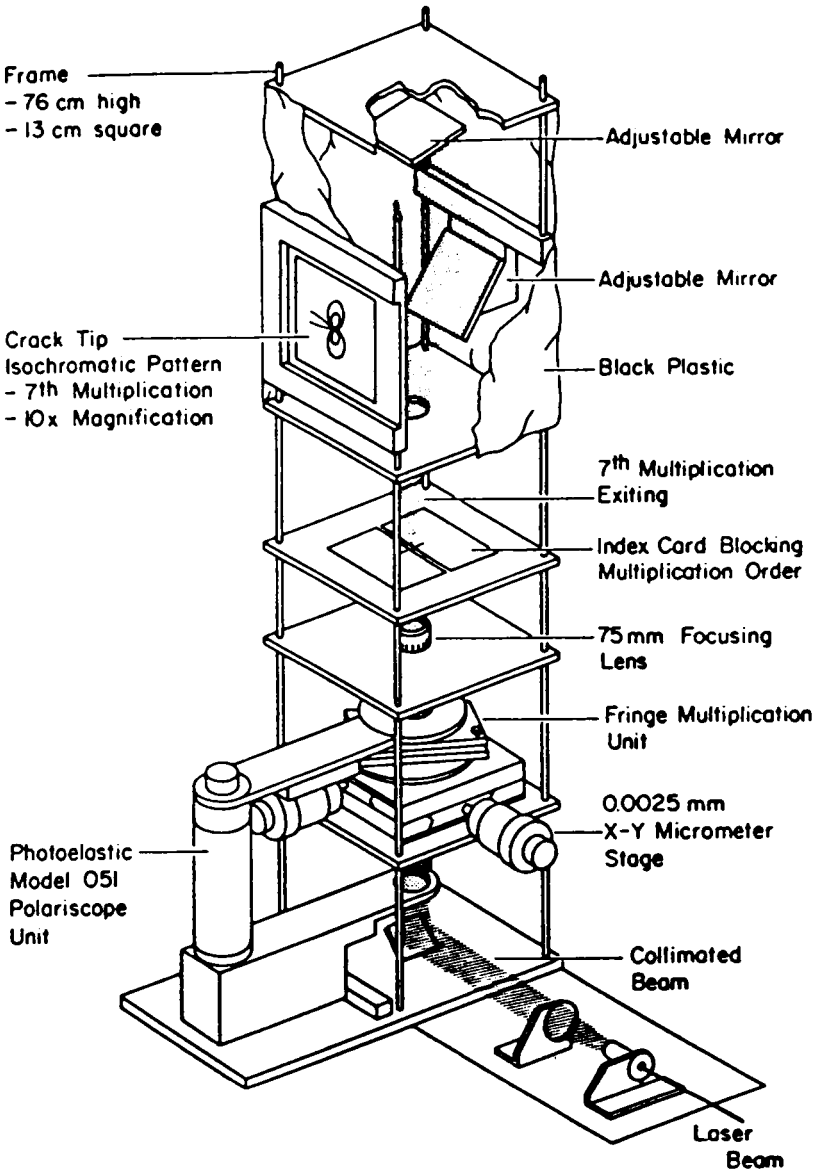

Figure 3.4. The fringe multiplier unit [46].

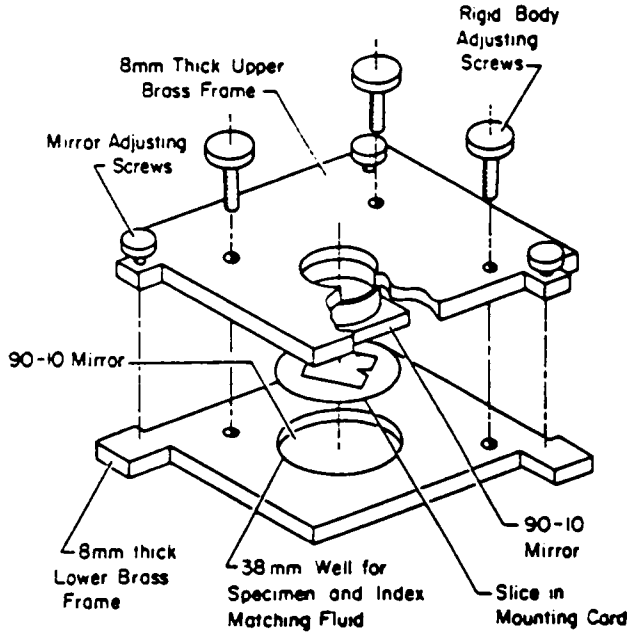

Figure 3.5. A blow up of the fixture used in the fringe multiplier unit [46].

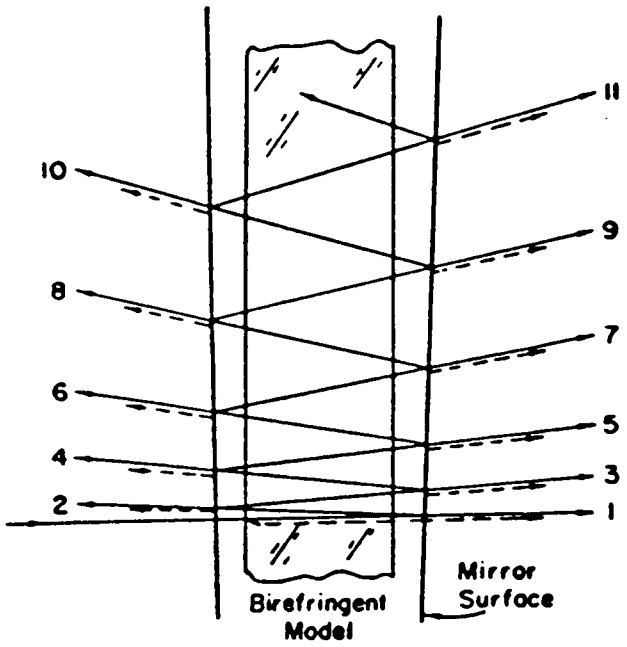

Figure 3.6. Sequence of multiplications of light leaving the partial mirrors [38].

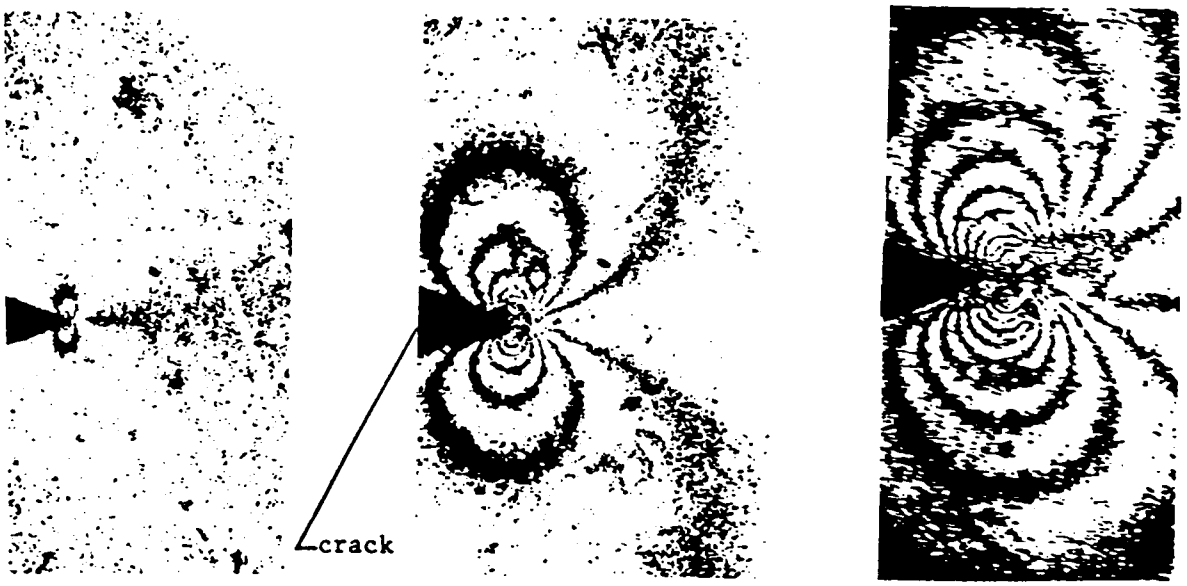

Figure 3.7. Multiplications of 1, 5, and 17 respectively [46].

3.5 Specimen Geometry and Preparation

3.5.1 Inert Propellant and Pure Binder

Each specimen was prepared in two phases. First the specimen was cut out of sheets to the geometry of biaxial specimens as shown in Fig. 3.8.

The specimen without the crack and rounded sides showed biaxial behavior at the center under tension. To assure the extension of the crack under load before the boundaries would crack, the sides were smoothed using a fine file. The grips were then glued using Kalex Uretha. The cement was a flexible, high peel strength adhesive provided by Hardman Inc., Belleville, N.J.. Insertion of the crack was very critical. Care was taken to assure a sharp crack tip. Two guides, and a knife made from a putty knife and custom cut in the shop, were used for this purpose. The sides of the knife were sharpened to give a sharp crack tip, and the guides led the knife into the specimen straight, resulting in a sharp, straight crack. The knife is shown in Fig. 3.9.

The second step was to transfer the grid to the surface. This process was covered in detail in the section describing the grid method.

3.5.2 Stress Freezing (PSM-9)

This material was cast in sheets of different thicknesses. The thickness of 0.5 in. (12.7 mm) was used for these tests. A beam of 1.12 x 11.12 in. (28.6 x 282.6 mm) was cut out of the sheet, using a band saw. The specimen was then trimmed to the actual size, 1 x 11 in. (25.4 x 279.4 mm), using a high speed router. This process resulted in very smooth sides without creation of any fringes due to heat. Then, using a guide, four holes with 0.25 in. (6.4 mm) diameter were

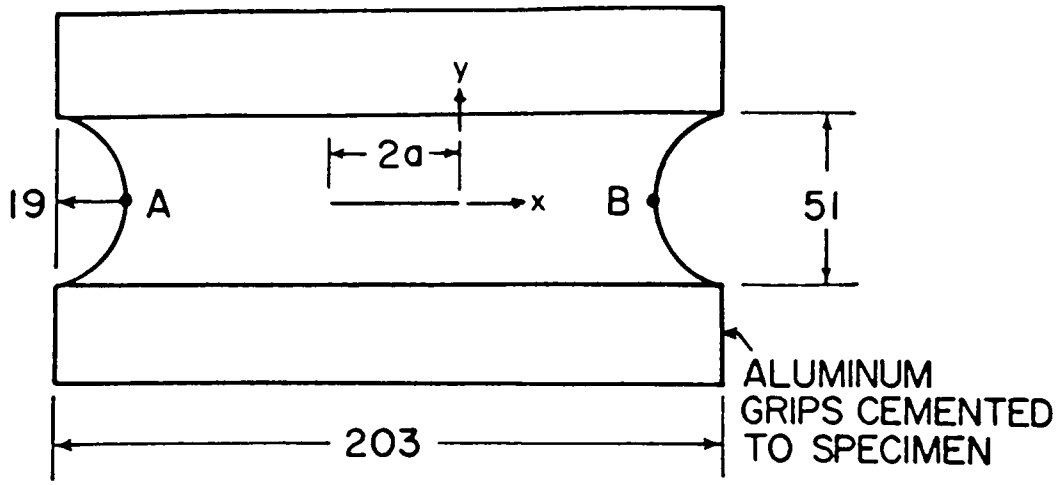

DIMENSIONS IN MILLIMETERS: INITIAL CRACK LENGTH ≈ 38 mm
SPECIMEN THICKNESS = 15.25 mm

Figure 3.8. The specimen geometry used for inert propellant and pure binder.

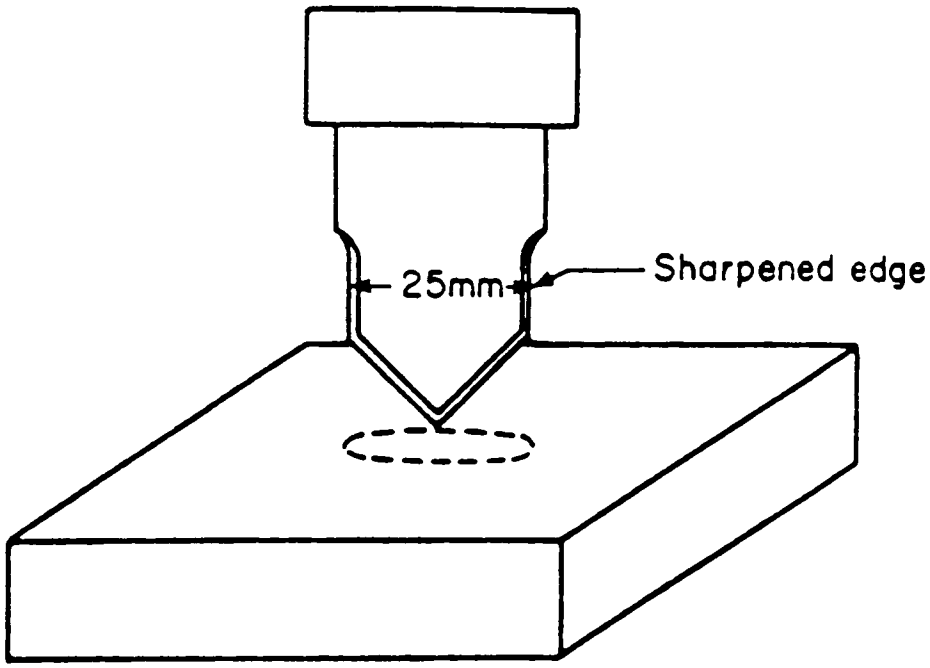

Figure 3.9. Method of inserting the initial crack in inert propellant and pure binder.

drilled as shown in Fig. 2.10. The next step was insertion of the crack. If a sharp artificial crack was desired, a band saw was used to drive the crack into the middle of the specimen to about 0.4 in. (10 mm) and then a special tool was used to extend the crack to half way through the width of the specimen. The tip of the crack had an included angle of 30° and root radius of less than 0.002 in. (0.05 mm). This would classify the crack as a sharp one. The crack border was straight and the angle between the crack border and the free surface was 90°. The details of dimensions are shown in Fig. 2.10.

If a natural crack was desired, the specimen would be prepared as explained above; then, using a band saw, a cut was made to 0.3 in. (7.6 mm). The end of the cut was extended by about 0.02 in. (0.5 mm) using a sharp X-acto knife. Then the specimen was put in the oven and enough load was monotonically added until the growth would start and reach the desired length. Then part of the load would be removed to arrest the crack. The resulting crack border in this case was usually a thumbnailed crack and the angle of the crack border with the free surface was different from 90°.

One point should be explained here to avoid confusion. When in this text the reader is referred to the "border" of a plane crack, it means a curve joining the loci of the crack front positions. The "profile" of the crack is a view of the opened crack at any point along the crack border when looking in a direction normal to a plane which is mutually orthogonal to the crack plane and its border

3.6 *Test Conditions*

After pure binder and inert propellant specimens were prepared, they were placed in a tensile machine. The displacements, strains, and dominant eigenvalue for displacement under ten-

sion were desired, so the specimens were loaded in tension normal to the crack plane at constant head rates. There was a question as to the influence of the rate of loading on the specimen deformation. To answer this question, two cross head speeds were chosen, one at 0.1 in./min (2.5 mm/min) and one at 1.0 in./min (25.4 mm/min). The record of load vs. time and extension vs. time were kept. Figure 3.10 shows the plot of load vs. time and extension vs. time for slow and fast rate of both pure binder and inert propellant [50]. Clearly the effect was significant over the range studied.

From a previous series of tests run in the laboratory, it was concluded that the absorption of moisture would alter the behavior of the material. So the material was kept in a sealed bag except for preparation or while the testing was performed.

The PSM-9 did not require any special consideration, except that it had to be soaked at the critical temperature for a few hours. The cooling process was not to exceed a rate of 3-5°F/hr., which was controlled automatically. The slicing process was to be done slowly and with the aid of coolant to avoid introduction of any new stress fringes due to heat.

3.7 Data Extraction

The data extraction procedure for inert propellant and pure binder was as follows:

A picture of the grid after it was transferred to the specimen, Fig. 3.1, was taken and used as the initial pattern. Then, as the specimen was loaded, new pictures were shot at different time intervals, using a 35mm camera [42], Fig. 3.11. The desired pictures were chosen and digitized. The reference was the crack tip and its plane. For displacements and strains, some grid lines were selected around the crack. The displacements were measured by the distance between the undeformed and deformed stages.

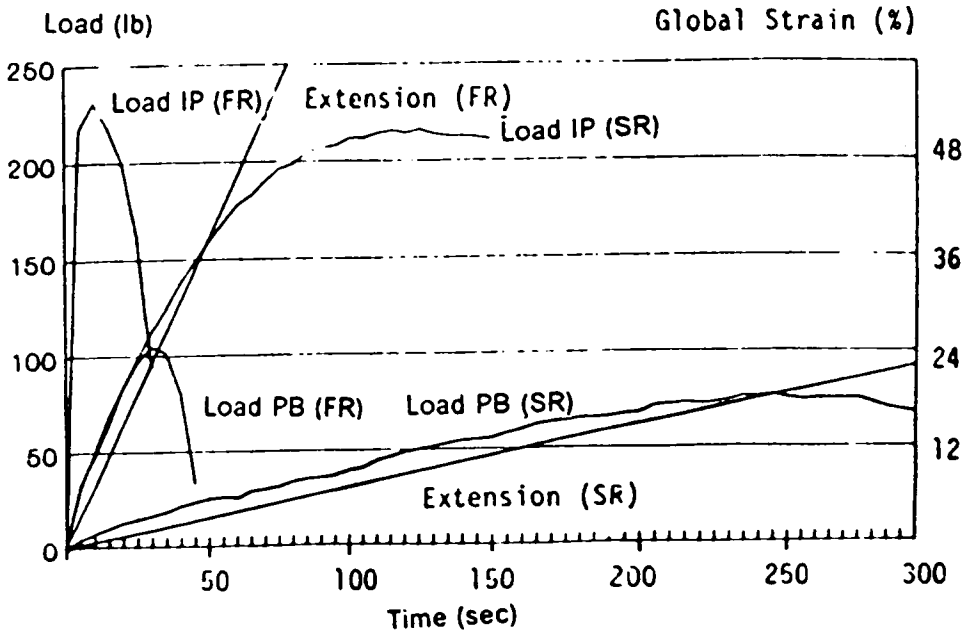

IP - Inert Propellant
PB - Pure Binder
SR - Slow Head Rate (2.54 mm/min)
FR - Fast Head Rate (25.4 mm/min)

Figure 3.10. Load-extension-time records for inert propellant and pure binder.

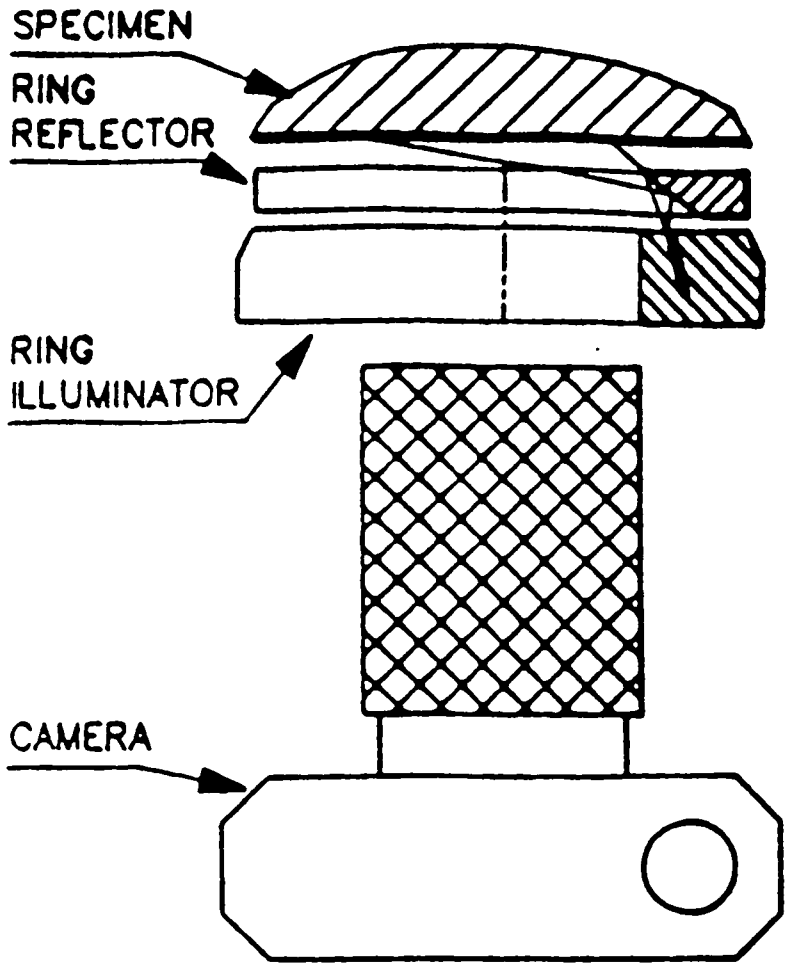

Figure 3.11. The set up used to photograph inert propellant and pure binder tests [42].

For the measurements of the dominant eigenvalue for displacement, data were taken along a line perpendicular to the crack plane. The points where horizontal and vertical lines of the grid crossed each other were used as points of interest and digitized. Figures 3.2 and 3.3 show the digitized points for one of the tests before and after load has been applied.

The data extraction for the PSM-9 was done by using the stage on the fringe multiplier unit. Tandem application of the Tardy method and fringe multiplication of five on the fringe multiplier unit gave about fifty data points. Again the data were collected at an angle 90° to the crack plane. The distance from the crack tip to the center of each fringe and the corresponding fringe number were collected and recorded. A typical fringe pattern is shown in Fig. 3.12.

For comparison purposes, the crack border and its angle with the free surface were to be photographed. For pure binder and inert propellant after some growth of the crack, a dye was shot into the specimen and, after completion of the test, the crack border was photographed. For PSM-9, in the case of an artificial crack, the crack border was a straight line, while for a natural crack the border was thumbnailed.

Figure 3.13 shows the crack front for pure binder and inert propellant. Figure 3.14 shows the crack front for the PSM-9 with natural crack.

Figure 3.13 shows that the angle of the crack border and the free surface is about 90° for inert propellant. This led to the conclusion that if the variation of the stress singularity is to be measured through the thickness of PSM-9 and used for inert propellant, the crack border similar to the one for inert propellant should be used.

For pure binder, Fig. 3.13, the crack border shows some retardation in the free surface after growth. The reason could be that insertion of the initial crack damaged the free surface.

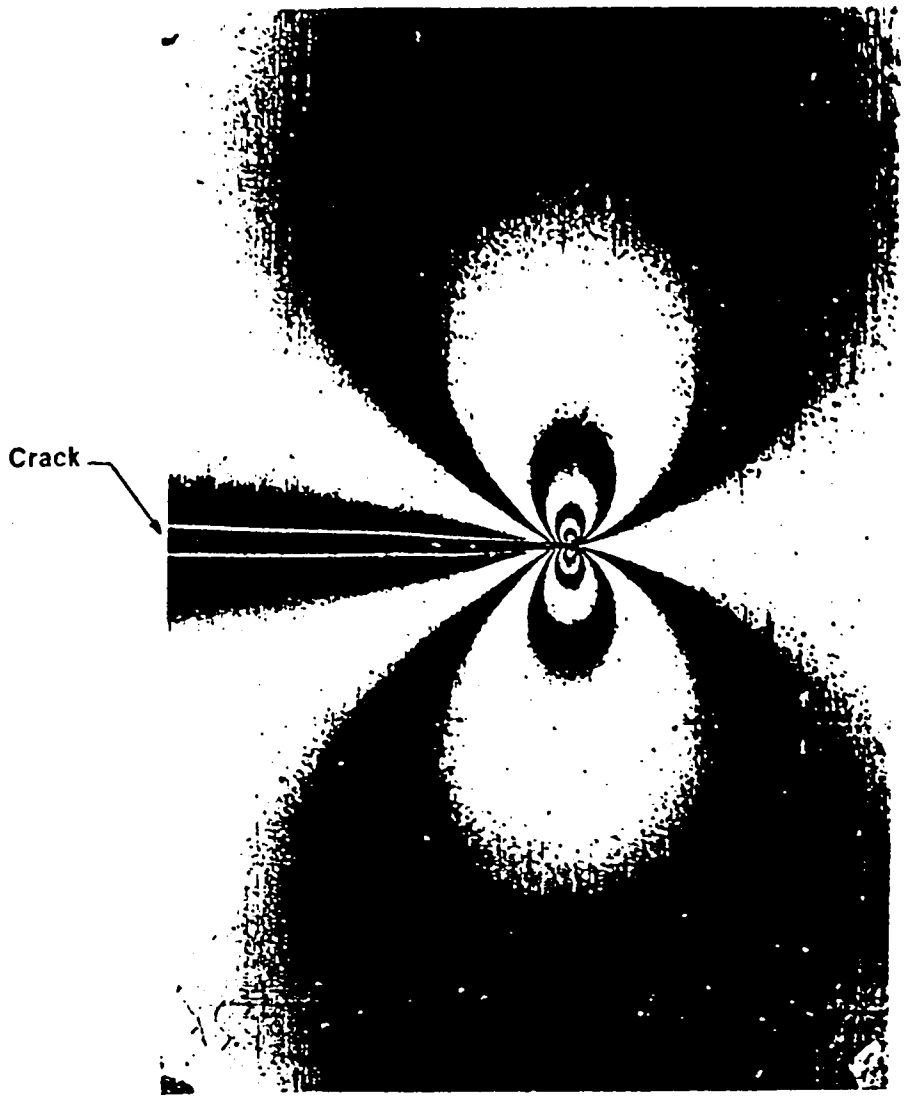

Figure 3.12. Typical stress fringe pattern for a cracked body in mode I.

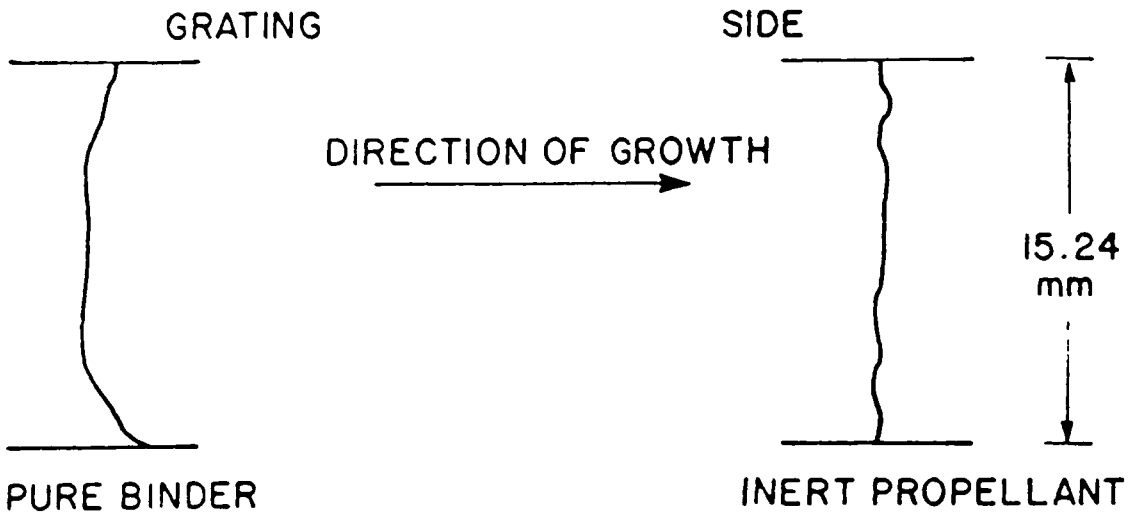

Figure 3.13. The crack border for inert propellant and pure binder after growth.

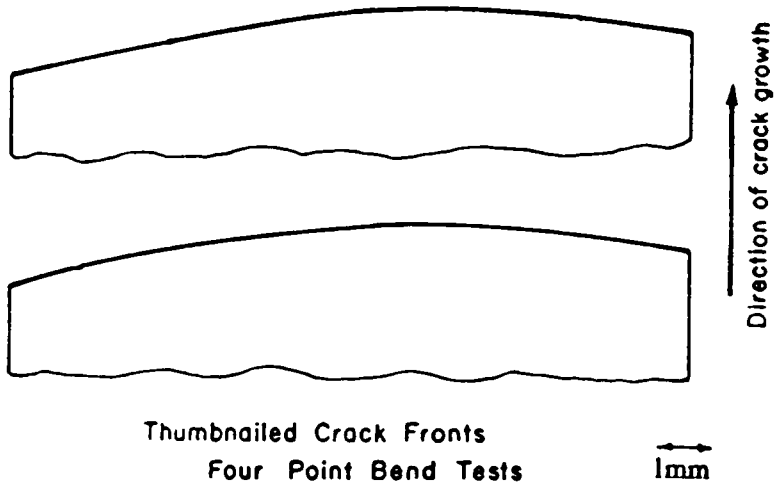

Figure 3.14. The crack border for natural cracks in four point bend tests.

4.0 Algorithms

4.1 Introduction

As was mentioned earlier, in the tests on pure binder and inert propellant the contours of displacements, strains, and the dominant eigenvalue for displacement were of interest for the case of inert propellant and pure binder.

For PSM-9, the variation through the thickness of the stress singularity for a crack with a straight front and a thumbnailed border were to be determined. The algorithms used for each of the above mentioned materials will be covered. For the stress and displacement eigenvalues, the two dimensional classical LEFM will be reviewed before the formulation for the free surface effect is presented.

4.2 Displacements and Strains for Pure Binder and Inert Propellant

For the digitizing process, two pictures are used, one before the deformation (giving an initial pattern), and one of the deformed grid. Points of interest were chosen around the initial crack tip with the initial crack tip as the reference point. These points were digitized in an array type manner and recorded for both pictures, i.e., the y position of each point was stored. The displacement in the y direction, U_2, is the difference between the y value of that specific point before and after loading. The formula below shows the mathematical form of the displacement in the y direction:

$$U_2 = Y_f - Y_i \tag{4.1}$$

Here 'i' refers to the initial, and 'f' to the final values digitized, Fig. 4.1.

Knowing the value of U_2 displacement around the crack tip, a computer code was developed to calculate the strain in the y direction, ε_y, using the formula shown below.

$$\varepsilon_y = \frac{\partial U_2}{\partial y} \tag{4.2}$$

4.3 Review of Mode I LEFM Algorithms for Displacement

Near tip equations can be derived [51] for displacements for the two dimensional case in the following forms:

$$U_1 = C_1 K_I G_x(\theta) r^{\frac{1}{2}} - \frac{\dot{\sigma}}{E_s} r \cos\theta \tag{4.3a}$$

$$U_2 = C_1 K_I G_y(\theta) r^{\frac{1}{2}} + \frac{\dot{\sigma}}{E_s} r \sin\theta \tag{4.3b}$$

where:

U_1 = displacement the in x-direction, (Fig. 4.1)

U_2 = displacement the in y-direction, (Fig. 4.1)

C_1 = constant, including elastic constants

$\dot{\sigma}$ = non-singular stress term

E_s = shear modulus

Considering zones close to the crack tip enables one to neglect the effect of the $\dot{\sigma}$ term, and reading data along $\theta = \frac{\pi}{2}$ reduces Eq. (4.3b) to:

$$U_2 = C_2 K_1 r^{\frac{1}{2}} \tag{4.4}$$

Sometimes, however, $\dot{\sigma}$ does make a contribution in the data zone, so one would use (along $\theta = \pi/2$):

$$U_2 = C_3 (K_1)_{AP} r^{\frac{1}{2}} \tag{4.5}$$

A plot of $\frac{U_2}{r^{\frac{1}{2}}}$ vs. $r^{\frac{1}{2}}$ would result in K_I. This analysis again assumes a displacement eigenvalue order of one half through the thickness. To account for the variation of the eigenvalue order, Benthem's analysis [14] was considered and modified to better represent the data for the particulate composite.

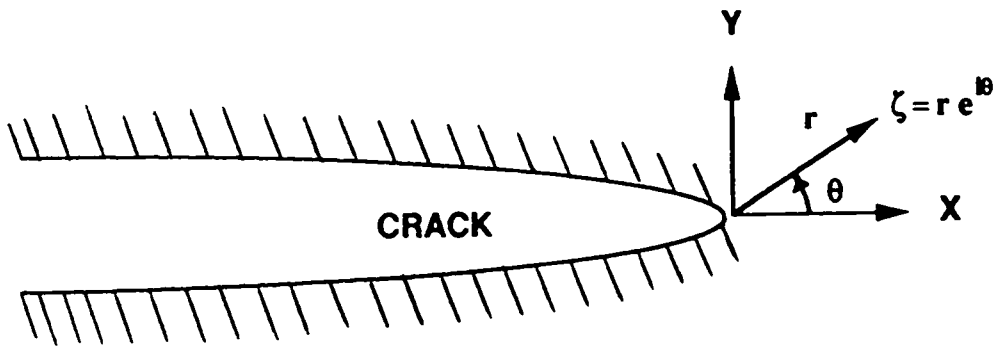

Figure 4.1. Near tip coordinate system.

4.4 Displacement Algorithm Taking Free Surface Effect into Consideration

Benthem assumed a separable eigenfunction series expansion form for displacements in the form of [14], (Fig. 2.5):

$$U_i = r^{\lambda_u^K} h_i(\theta, \phi)_K \qquad K = 1, \ldots, \infty \tag{4.6}$$

where:

U_i = displacement (i = 1, 2)

λ_u^k = eigenvalue

$h_i(\theta, \phi)$ = eigenfunction

As before, considering the leading term and taking data along $\theta = \frac{\pi}{2}$ and $\phi = \frac{\pi}{2}$ results in :

$$U_2 = D_2 r^{\lambda_u} \tag{4.7}$$

Taking the natural log of both sides, there results:

$$\ln(U_2) = \ln(D_2) + \lambda_u \ln(r) \tag{4.8}$$

Thus λ_u is the slope of the $\ln(U_2)$ vs. $\ln(r)$.

For the case of inert propellant, blunting was observed at the crack tip, Fig. 4.2. The amount of blunting, $2U_0$, was carefully measured and taken into consideration in Eqn. (4.8).

The revised form is as written below:

$$U_2 = D_2 r^{\lambda_u} + U_0 \tag{4.9}$$

$$\ln(U_2 - U_0) = \ln(D_2) + \lambda_u \ln(r) \tag{4.10}$$

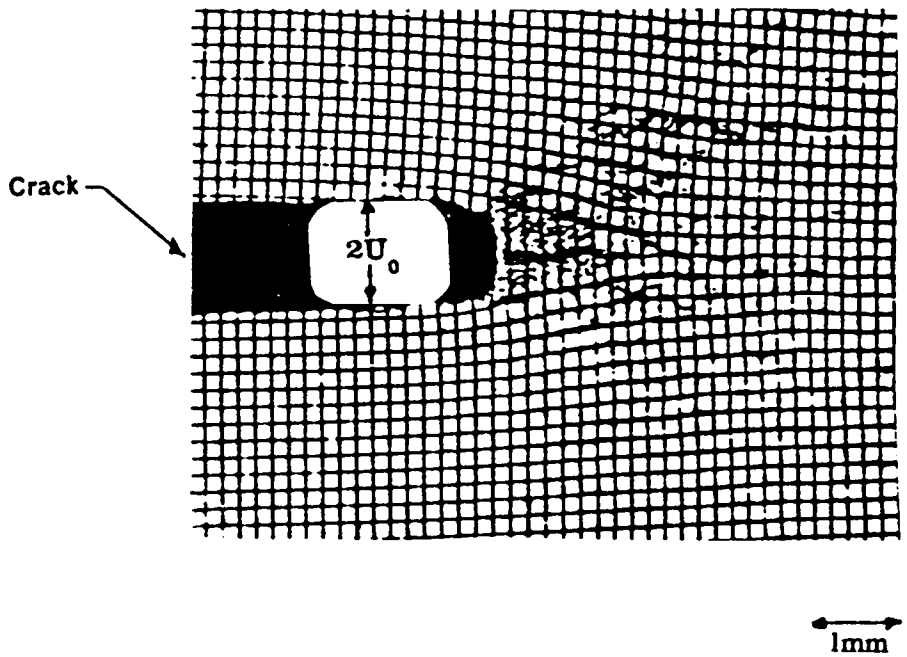

Figure 4.2. Grid with value of $2U_0$ shown.

4.5 Review of Mode I LEFM Algorithms for Photoelastic Data

The LEFM assumes a square root singularity order of one half and it ignores the highly three dimensional effect near and at the surface of the specimen. Then the two dimensional state of stress in regions affected by the singularity is [43], Fig. 4.1:

$$\sigma_{ij} = \frac{K_I}{(2\pi r)^{\frac{1}{2}}} f_{ij}(\theta) - \dot{\sigma}_{ij}(\theta) \qquad i,j = x,y \tag{4.11}$$

where:

σ_{ij} = near-tip in plane singular stress components

K_I = Mode I Stress Intensity Factor (SIF)

$\dot{\sigma}_{ij}$ = near-tip contribution of non-singular stresses

The above equation can be written out in the form shown below (Fig. 4.1):

$$\sigma_{xx} = \frac{K_I}{(2\pi r)^{\frac{1}{2}}} \cos\frac{\theta}{2}\left[1 - \sin\frac{\theta}{2}\sin\frac{3\theta}{2}\right] - \dot{\sigma} \tag{4.12a}$$

$$\sigma_{yy} = \frac{K_I}{(2\pi r)^{\frac{1}{2}}} \cos\frac{\theta}{2}\left[1 + \sin\frac{\theta}{2}\sin\frac{3\theta}{2}\right] \tag{4.12b}$$

$$\sigma_{xy} = \frac{K_I}{(2\pi r)^{\frac{1}{2}}} \left[\sin\frac{\theta}{2}\cos\frac{\theta}{2}\cos\frac{3\theta}{2}\right] \tag{4.12c}$$

Recall the definition for maximum shearing stress:

$$\tau_{max}^2 = \frac{1}{4}\{(\sigma_{xx} - \sigma_{yy})^2 + 4\sigma_{xy}^2\} \tag{4.13}$$

Substitution of Eqns.(4.12) into Eqn.(4.13) yields Eqn.(4.14) along $\theta = \frac{\pi}{2}$.

$$\tau_{max}^2 = \frac{K_I^2}{8\pi r} + \frac{k_I \dot{\sigma}}{4(\pi r)^{\frac{1}{2}}} + \frac{(\dot{\sigma})^2}{4} \tag{4.14}$$

which when combined with the stress-optic law [45]:

$$\tau_{max} = \frac{nf}{2t} \tag{4.15}$$

where:

n = photoelastic fringe order

f = material fringe value

t = thickness of specimen

yields an expression for K_I, as shown below:

$$K_I = (\pi r)^{\frac{1}{2}} \{[2(\frac{nf}{t})^2 + (\dot{\sigma})^2]^{\frac{1}{2}} - \dot{\sigma}\} \tag{4.16}$$

Assuming $(\dot{\sigma})^2$ to be small relative to $8\tau_{max}^2 (= 2(\frac{nf}{t})^2)$, and rearranging Eqn.(4.16), results in [53]:

$$\tau_{max} = \frac{K_I}{(8\pi r)^{\frac{1}{2}}} + \frac{\dot{\sigma}}{\sqrt{8}} \tag{4.17}$$

Defining apparent SIF as:

$$(K_I)_{AP} = \tau_{max}(8\pi r)^{\frac{1}{2}} \tag{4.18}$$

and normalizing with respect to $\bar{\sigma}(\pi a)^{\frac{1}{2}}$ where:

$\bar{\sigma}$ = remote stress

a = half of crack length

results in:

$$\frac{(K_I)_{AP}}{\bar{\sigma}(\pi a)^{\frac{1}{2}}} = \frac{K_I}{\bar{\sigma}(\pi a)^{\frac{1}{2}}} + \frac{\dot{\sigma}}{\bar{\sigma}}\left(\frac{r}{a}\right)^{\frac{1}{2}} \tag{4.19}$$

Equation (4.19) describes a linear relationship between $\left(\frac{r}{a}\right)^{\frac{1}{2}}$ and $\frac{(K_I)_{AP}}{\bar{\sigma}(\pi a)^{\frac{1}{2}}}$.

From a variety of tests, a linear zone of $\left(\frac{r}{a}\right)^{\frac{1}{2}}$ from 0.2 to 0.4 has been established. One could extrapolate back to the vertical axis for values of the normalized K_I.

4.6 Photoelastic Algorithm Taking Free Surface Effect into Consideration

One can use a complex stress function with a variable first eigenvalue to define the three dimensional stress state near the free surface boundary layer near the crack tip. This would be equivalent to applying a quasi two dimensional stress state to slices removed in that boundary layer.

If one assumes an analytic function z in the form shown below, x and y can be obtained as the Re(z) and Im(z), respectively, as shown below [38,55]:

$$z = x + iy \tag{4.20}$$

This would lead to:

$$\sigma_{xx} = Re(z) - Im(z) \tag{4.21a}$$

$$\sigma_{yy} = Re(z) + yIm(z) \tag{4.21b}$$

$$\sigma_{xy} = -yRe(z') \tag{4.21c}$$

where:

$$Re(z') = \frac{\partial Re(z)}{\partial x} = \frac{\partial Im(z)}{\partial y} \tag{4.22}$$

As in LEFM, we can assume a two dimensional stress function $f(\zeta)$ in the form of:

$$Z = \frac{f(\zeta)}{\zeta^{\lambda_\sigma}} \tag{4.23}$$

in which λ_σ is the stress singularity order. ζ is equal to $(re^{i\theta})$ and originates at the crack tip as shown in Fig. 4.1. Expanding $f(\zeta)$ in a MacLaurin series about the crack tip and at the same time letting ζ approach zero, one would get:

$$f(\zeta) = \frac{K_{\lambda_\sigma}}{\sqrt{2\pi}} + a_1\zeta + a_2\zeta^2 + \cdots \tag{4.24}$$

$$Z\Big|_{|\zeta| \to 0} = \frac{K_{\lambda_\sigma}}{\sqrt{2\pi}} r^{-\lambda}\sigma \tag{4.25}$$

It should be noted that if λ_σ is set equal to its classical value of 0.5, LEFM would be recovered. Now if one substitutes Eqn.(4.25) into Eqns.(4.21), one would get the following equations for stresses:

$$\sigma_{xx} = \frac{K_{\lambda_\sigma}}{\sqrt{2\pi}\, r^{\lambda_\sigma}} \{\cos \lambda_\sigma\theta - \lambda_\sigma \sin\theta \sin(\lambda_\sigma + 1)\theta\} - \dot{\sigma} \tag{4.26a}$$

$$\sigma_{yy} = \frac{K_{\lambda_\sigma}}{\sqrt{2\pi}\, r^{\lambda_\sigma}} \{\cos \lambda_\sigma\theta + \lambda_\sigma \sin\theta \sin(\lambda_\sigma + 1)\theta\} \tag{4.26b}$$

$$\sigma_{xy} = \frac{K_{\lambda_\sigma}}{\sqrt{2\pi}\, r^{\lambda_\sigma}} \{\lambda_\sigma \sin\theta \cos(\lambda_\sigma + 1)\theta\} \tag{4.26c}$$

where:

K_{λ_σ} = stress eigenfactor.

$\lambda\sigma$ = stress singularity which is different from $\frac{1}{2}$.

Upon substitution of Eqns. (4.26) into Eqn. (4.13) and assuming $\frac{\dot{\sigma}(2\pi)^{\frac{1}{2}} r^{\lambda_\sigma}}{K_{\lambda_\sigma}\lambda_\sigma \sin\theta} < 1$, one obtains [54]:

$$\tau_{max} = \frac{\lambda_\sigma K_{\lambda_\sigma} \sin\theta}{\sqrt{2\pi}\, r^{\lambda_\sigma}} + \frac{\dot{\sigma}}{2} \sin(\lambda_\sigma + 1)\theta \tag{4.27}$$

Again, along $\theta = \frac{\pi}{2}$ the above equation reduces to:

$$\tau_{max} = \lambda_\sigma \frac{K_{\lambda_\sigma}}{\sqrt{2\pi}\, r^{\lambda_\sigma}} + \frac{\dot{\sigma}}{2} \sin(\lambda_\sigma + 1)\frac{\pi}{2} = \lambda_\sigma \frac{(K_{\lambda_\sigma})_{AP}}{\sqrt{2\pi}\, r^{\lambda_\sigma}} \tag{4.28}$$

There remains the task of measuring $\dot{\sigma}$. Away from the free surface, a state of plane strain would dominate and the singularity of $\frac{1}{2}$ prevails. So if one plots $\frac{(K_I)_{AP}}{\bar{\sigma}\sqrt{\pi a}}$ vs. $\sqrt{\frac{r}{a}}$, the slope would be τ_0,

$$\tau_0 = \frac{\dot{\sigma}}{2} \sin(\lambda_\sigma + 1)\frac{\pi}{2} \tag{4.29}$$

Equation (4.29) leads to the conclusion that as one moves from the state of plane strain, near the center portion of the specimen, to the free surface, the singularity would vary from $\frac{1}{2}$ to λ_σ. So τ_0 should change as well.

The approach here is to assume a constant value of τ_0 for the inside region, where plane strain governs, and a linear variation of τ_0 up to the free surface. Since without any correction the value of the singularity at the free surface was the same as Benthem's analytical solution as

well as the experimental value using moire, the free surface was assigned a value of zero for the τ_0. With the determination of τ_0, Eqn. (4.28) reduces to:

$$\tau_{max} = \lambda_\sigma \frac{K_{\lambda_\sigma}}{\sqrt{2\pi}\, r^{\lambda_\sigma}} + \tau_0 \tag{4.30}$$

Taking τ_0 to the left hand side of Eqn. (4.30) and taking the natural log. of both sides, results in:

$$\ln(\tau_{max} - \tau_0) = \ln(\lambda_\sigma \frac{K_{\lambda_\sigma}}{\sqrt{2\pi}}) - \lambda_\sigma \ln r \tag{4.31}$$

Again the result would be a line with horizontal axis as $\ln r$ and vertical axis as $\ln(\tau_{max} - \tau_0)$, leading to a slope of λ_σ.

5.0 Results

5.1 Pure Binder Results

After preparation of the specimens, as was covered in detail in previous chapters, they were placed in the tensile machine and pulled in tension. A total of six tests were run and analyzed. Tests numbered 1, 2, 3, and 4 were run at a rate of 0.1 in./min (2.5 mm/min), and the rate for tests 3 and 4 was 1.0 in./min (25.4 mm/min). The rate is defined as the speed at which grips were pulled away from each other, i.e., the global separation rate of the two grips.

Pictures were taken before the loading process started and at set time intervals while the test was in progress. Figure 5.1 shows a sequence of these photographs for the slow rate. The sequence shows pictures of the grid before loading and after loading starts, and includes stages of crack opening and crack extension. The load vs. time and extension vs. time relations were also recorded, and a plot of them is shown in Fig. 3.10. The contour maps of displacements and strains in the y direction are shown in Fig. 5.2. The crack border for slow rate and fast rate had the same shape and is shown in Fig. 3.13. The dominant displacement

eigenvalues were calculated for several different global strain levels for each test and are tabulated in table 5.1.

Since the pure binder had a high Poisson's ratio, the value of the dominant displacement eigenvalue at the free surface was expected to be significantly different from the classical value of one half. Indeed, it had an average value of 0.63 which favorably compared with Benthem's value.

The fast rate tests performed on pure binder showed the same general behavior as the slow rate. Figure 5.3 shows a series of pictures before loading started and afterwards. The crack border was again straight with some retardation at the free surface. Table 5.2 gives the values of the dominant displacement eigenvalue measured at the free surface for tests 5 and 6.

The algorithms for calculating the eigenvalue for displacement were covered earlier. Referring to the pictures of the crack profiles, one would conclude that the tip of the crack is smooth enough to lead to the conclusion that $2U_0$ (the blunting ahead of the crack tip) could be set equal to zero. In this case, the utilization of Eqn. 4.10 of the text with $U_0 = 0$ results in Eqn. 4.8 and a plot of $\ln(U_2)$ vs. $\ln(r)$ yields a line whose slope is the dominant eigenvalue for displacement. Figures 5.4 and 5.5 show a plot of the dominant eigenvalue for displacement for slow and fast rate, respectively.

5.2 *Inert Propellant Results*

The preparation and loading process was the same as for pure binder. For inert propellant a total of four tests were run. Tests 1 and 2 used a global head rate of 0.1 in./min (2.5 mm/min), and tests 3 and 4 used a global head rate of 1.0 in./min (25.4 mm/min). The behavior near the

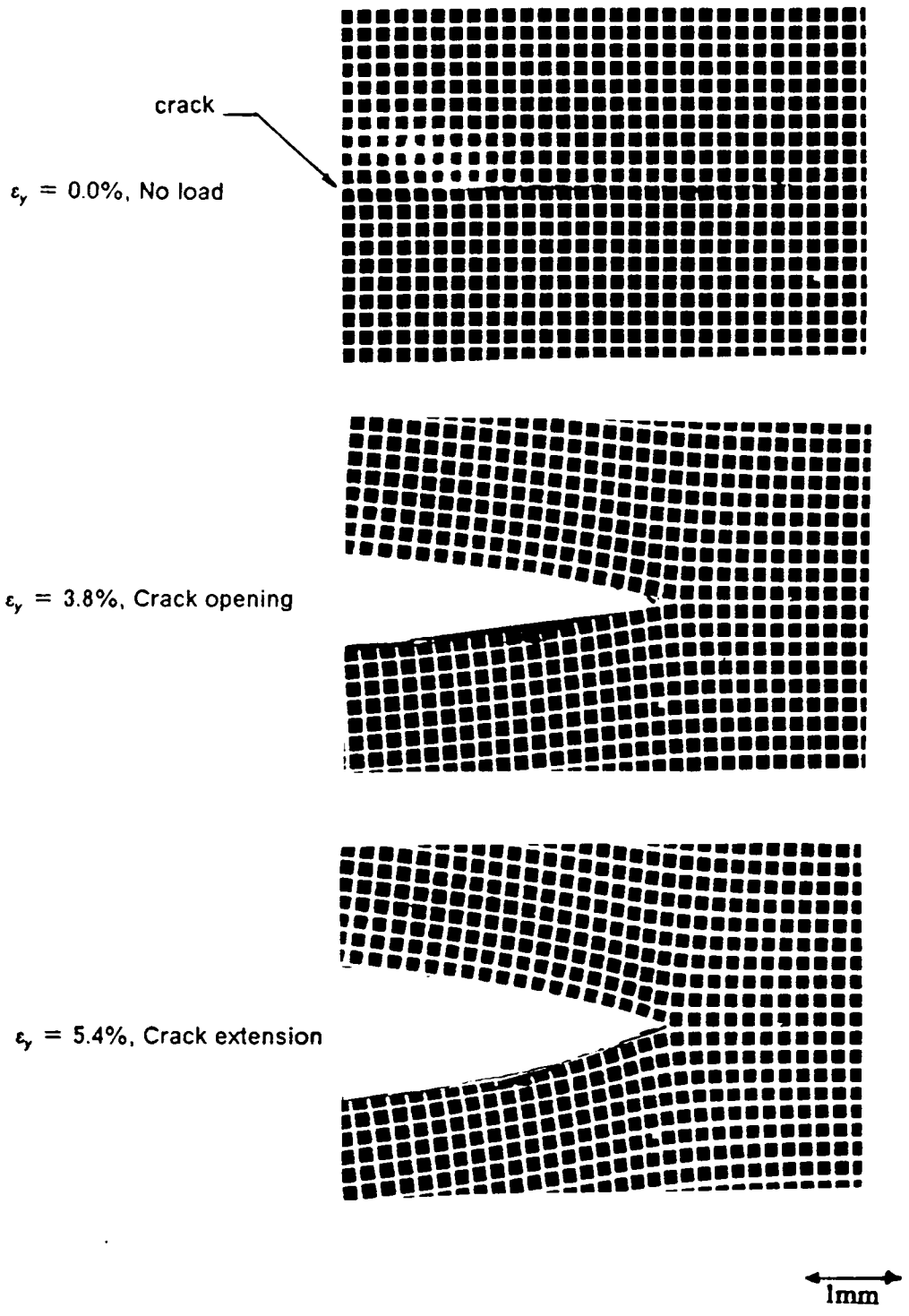

Figure 5.1. A series of pictures for pure binder, slow rate.

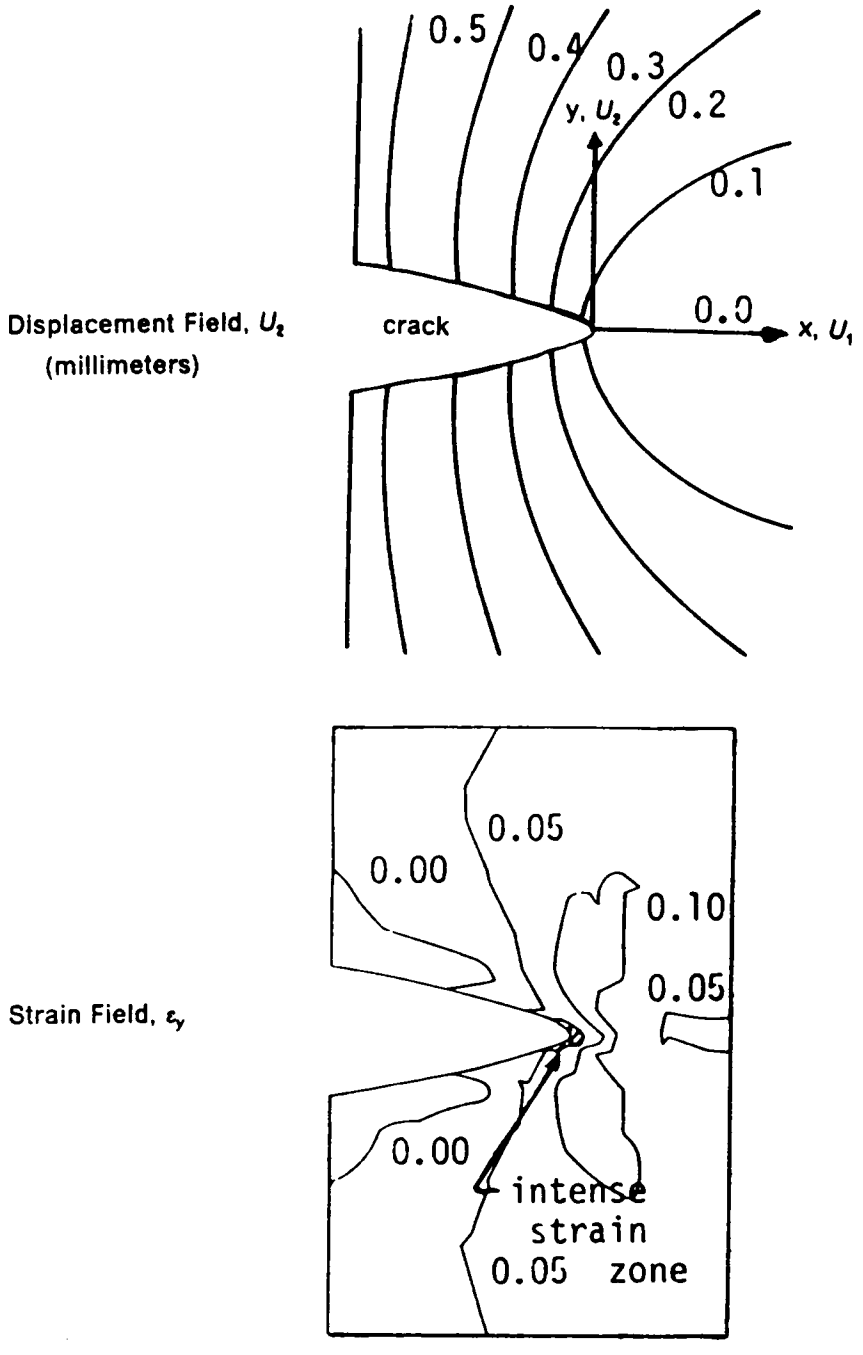

Figure 5.2. Contour of displacements and strains in the y direction for pure binder, slow rate.

Table 5.1. The dominant eigenvalue for displacement for pure binder tests.

Test 1		Test 2	
Linear Zone (range) = 2.0-6.0 mm Displacement Rate = 2.5 mm/min $2U_0 = 0$ mm		Linear Zone (range) = 1.5-5.0 mm Displacement Rate = 2.5 mm/min $2U_0 = 0$ mm	
ε%	λ_u	ε%	λ_u
1.94 3.49 5.06 6.60 9.74 17.35	.727 .628 .569 .597 .568 .597	.37 1.93 3.47 12.87 17.36	.748 .730 .737 .631 .670
λ_u (avg) = .614		λ_u (avg) = .703	

Test 3		Test 4	
Linear Zone (range) = 1.5-5.0 mm Displacement Rate = 2.5 mm/min $2U_0 = 0$ mm		Linear Zone (range) = 1.5-5.0 mm Displacement Rate = 2.5 mm/min $2U_0 = 0$ mm	
ε%	λ_u	ε%	λ_u
4.68 6.24 7.80 12.52	.595 .587 .580 .534	7.03 10.55 12.92 15.30 17.36%	.641 .608 .556 .566 .602
λ_u (avg) = .574		λ_u (avg) = .595	

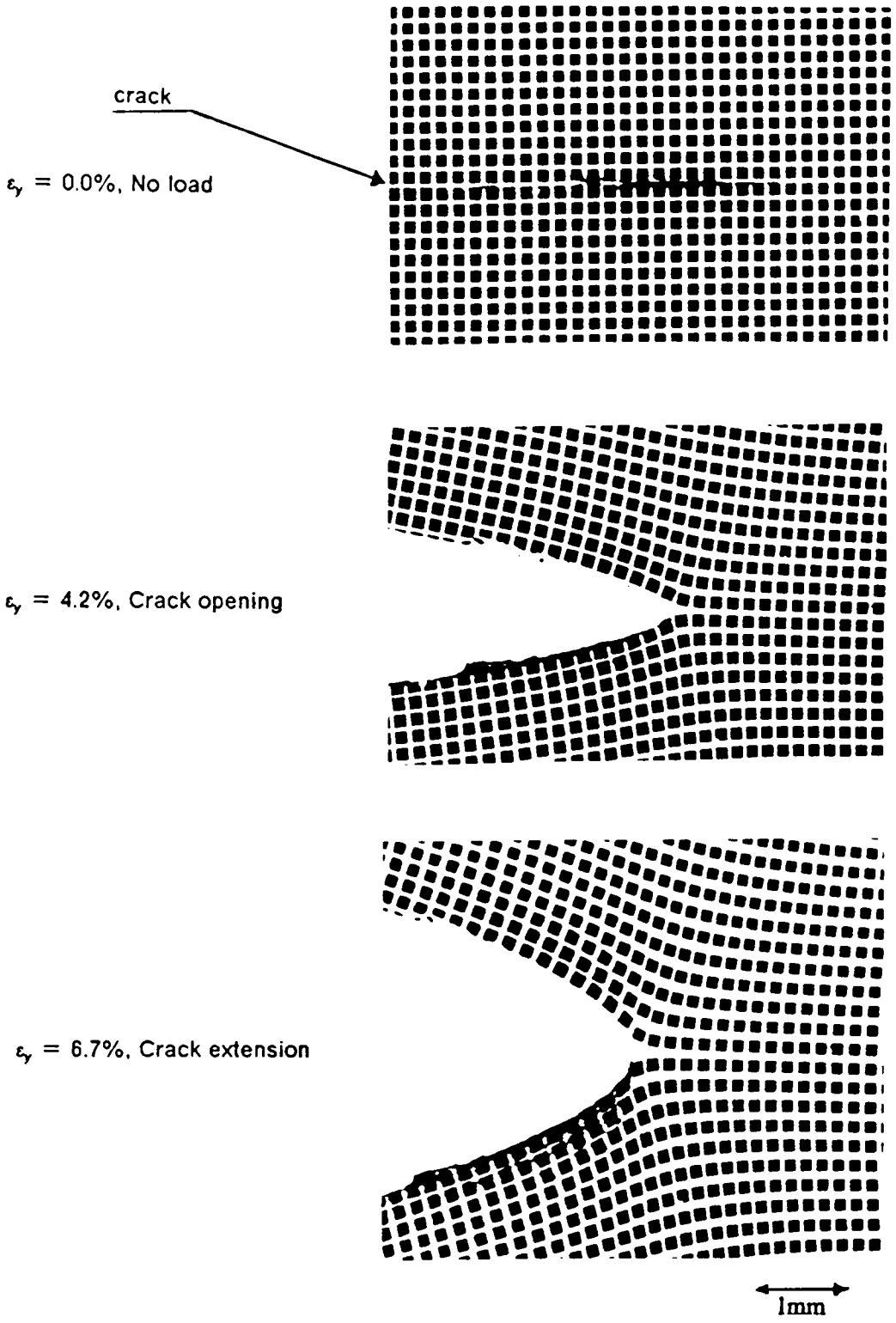

Figure 5.3. A series of photographs for pure binder, fast rate.

Table 5.2. The dominant eigenvalue for displacement for pure binder tests.

Test 5		Test 6	
Linear Zone (range) = 1.0-6.0 mm Displacement Rate = 25.4 mm/min $2U_0 = 0$ mm		Linear Zone (range) = 1.5-5.0 mm Displacement Rate = 25.4 mm/min $2U_0 = 0$ mm	
ε%	λ_u	ε%	λ_u
1.65	.807	6.40	.749
3.24	.642	8.00	.722
6.41	.569	11.20	.660
7.98	.573	12.80	.668
12.80	.526		
16.05	.556		
λ_u (avg) = .612		λ_u (avg) = .700	

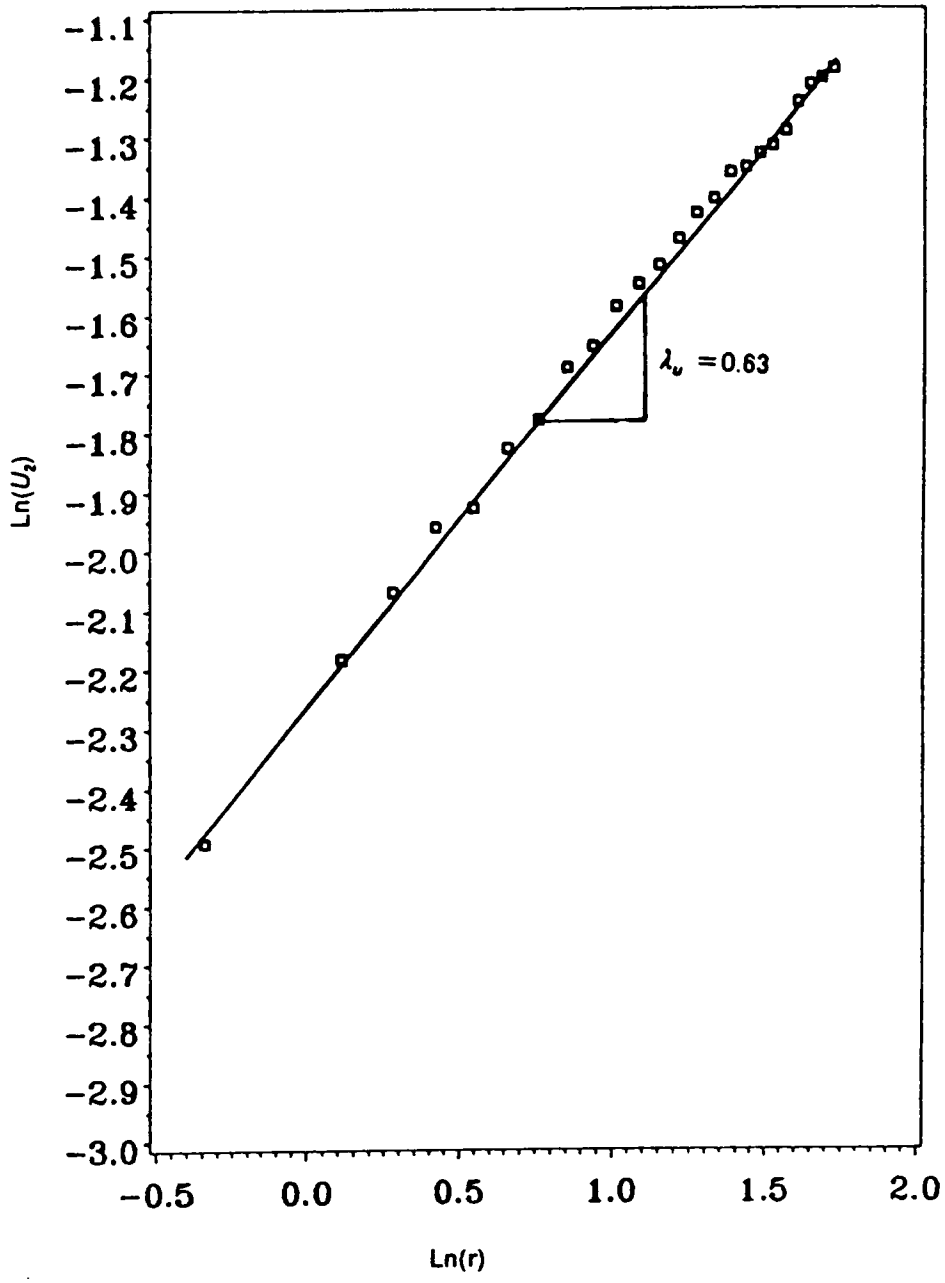

Figure 5.4. Plot of displacement eigenvalue for pure binder, slow rate.

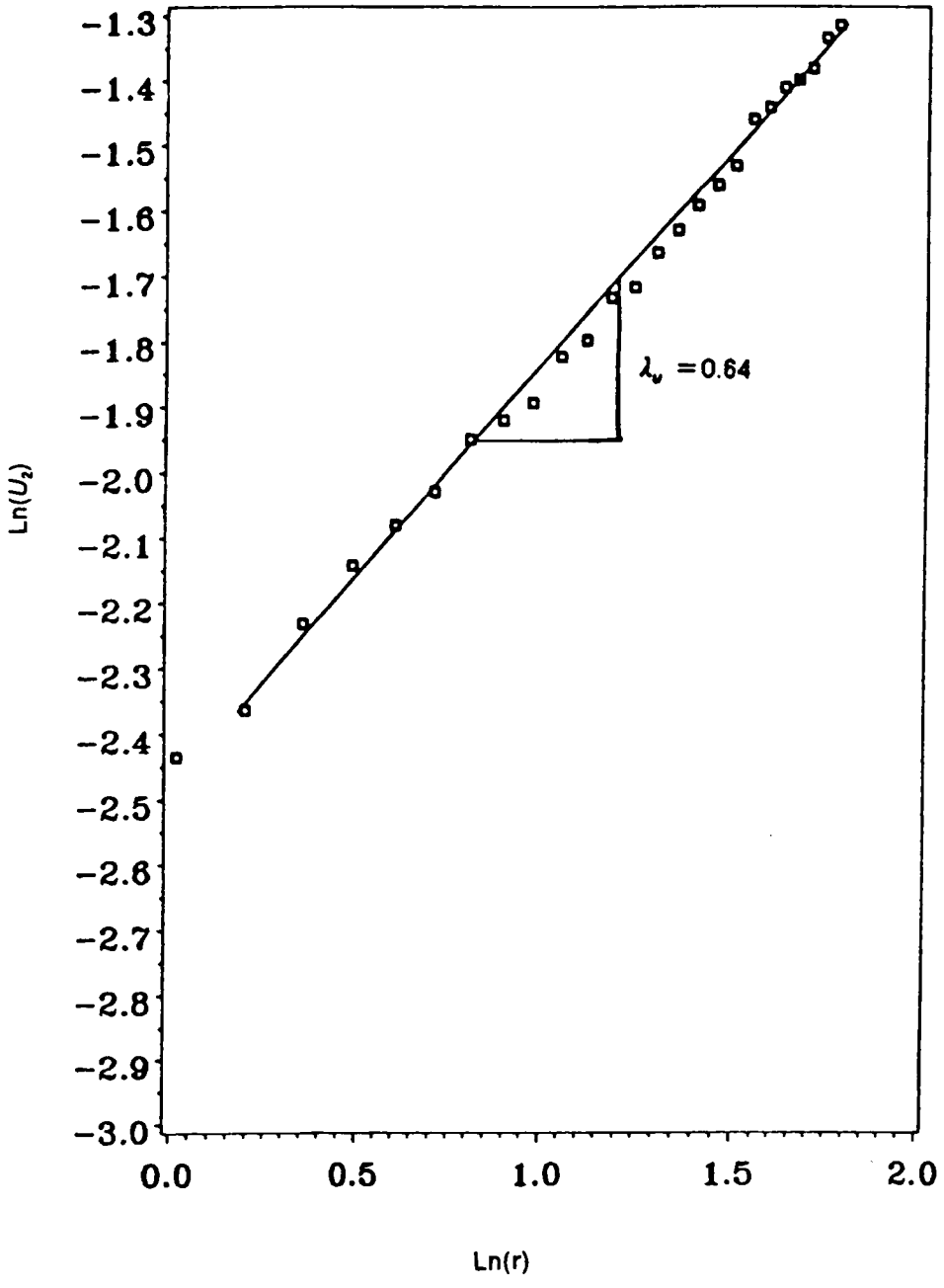

U_2 and r in millimeters

Figure 5.5. Plot of displacement eigenvalue for pure binder, fast rate.

crack tip was different in inert propellant; due to rigid particles, the crack showed some blunting at the crack tip. The process was usually a combination of opening, blunting, creation of void ahead of the crack tip, and connection of the crack to the void to extend the crack. The last section of this chapter elaborates more on this process.

Figures 5.6 and 5.7 show a series of pictures for the slow and fast rate, respectively. The amount of blunting is well defined in these pictures. The displacements and strains in the y direction for the slow rate is shown in Fig. 5.8.

Comparing the strains in the y direction for pure binder and inert propellant reveals that inclusion of the particles would result in an intensive strain zone ahead of the crack tip for inert propellant. This would force the inner limit of the linear zone for the displacement eigenvalue measurements to be farther out for inert propellant relative to pure binder.

To measure the dominant eigenvalue for displacement, Eqn. 4.10 was used. The value of $2U_0$ was accurately measured and taken into account in the calculations. Figures 5.9 and 5.10 show a typical plot of Eqn. 4.10, with the slope being the displacement eigenvalue for slow and fast rates, respectively. The crack tip profile for inert propellant at a certain strain level for the fast rate is shown in Fig. 5.11 for a better understanding of $2U_0$ and comparison purposes with pure binder. Tables 5.3 and 5.4 list the displacement eigenvalues for tests 1, 2 (slow rate), and 3, 4 (fast rate), respectively. These numbers in average compare reasonably well with the analysis carried out by other researchers such as Benthem.

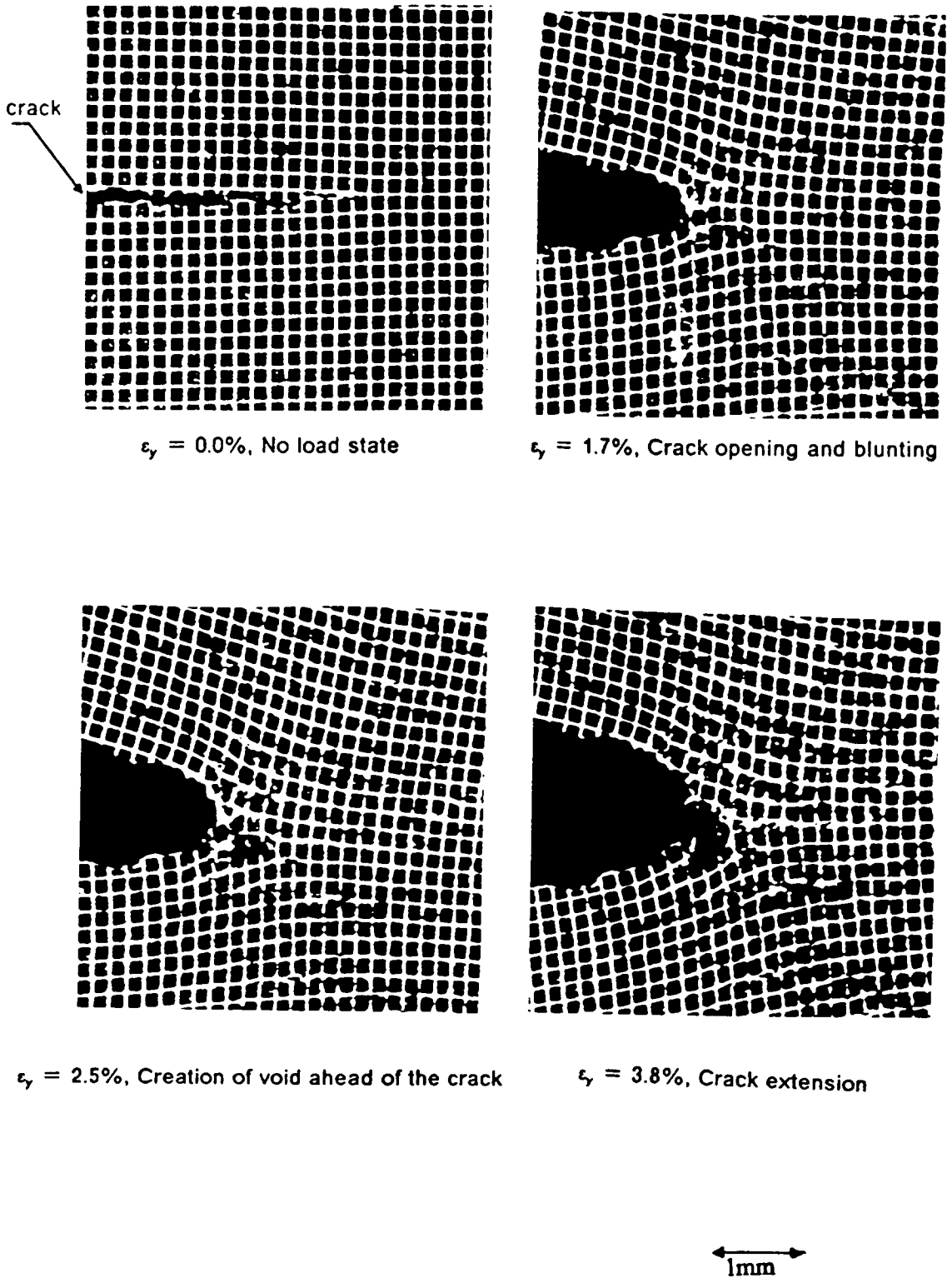

Figure 5.6. A series of pictures on inert propellant, slow rate.

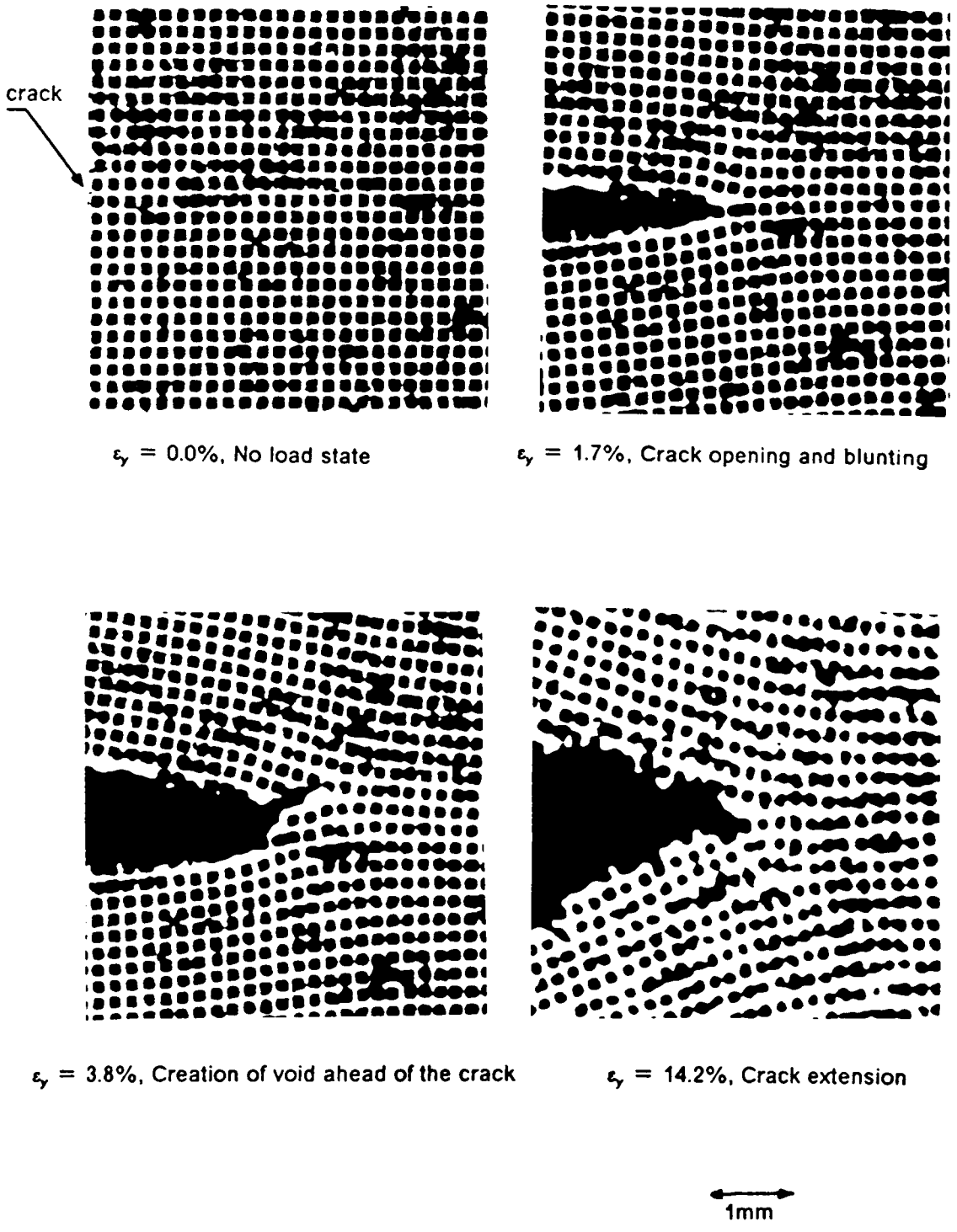

Figure 5.7. A series of pictures on inert propellant, fast rate.

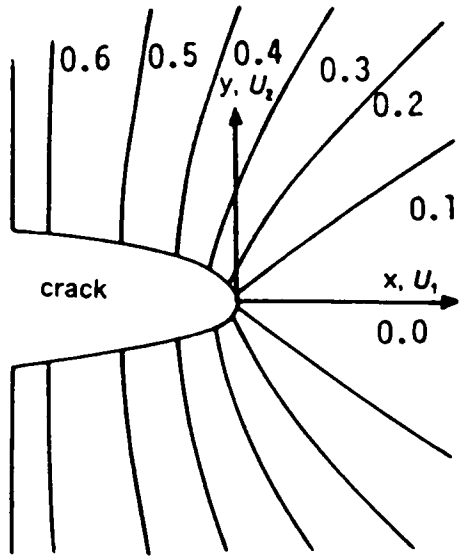

Displacement Field, U_2
(millimeters)

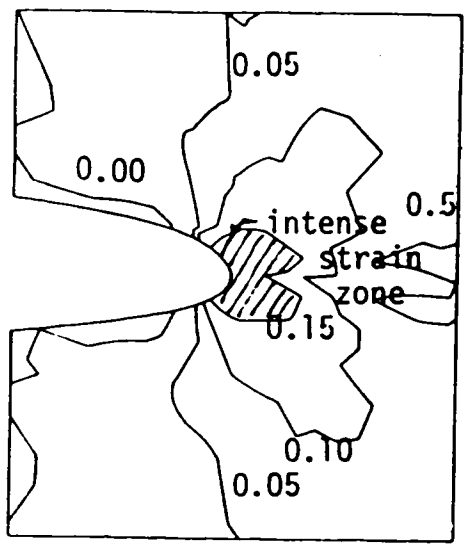

Strain Field, ε_y

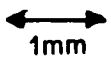

Inert Propellant
Head Rate = 2.5mm/min
Global Strain, ε_y = 4.0%

Figure 5.8. Contour of displacements for and strains for inert propellant, slow rate.

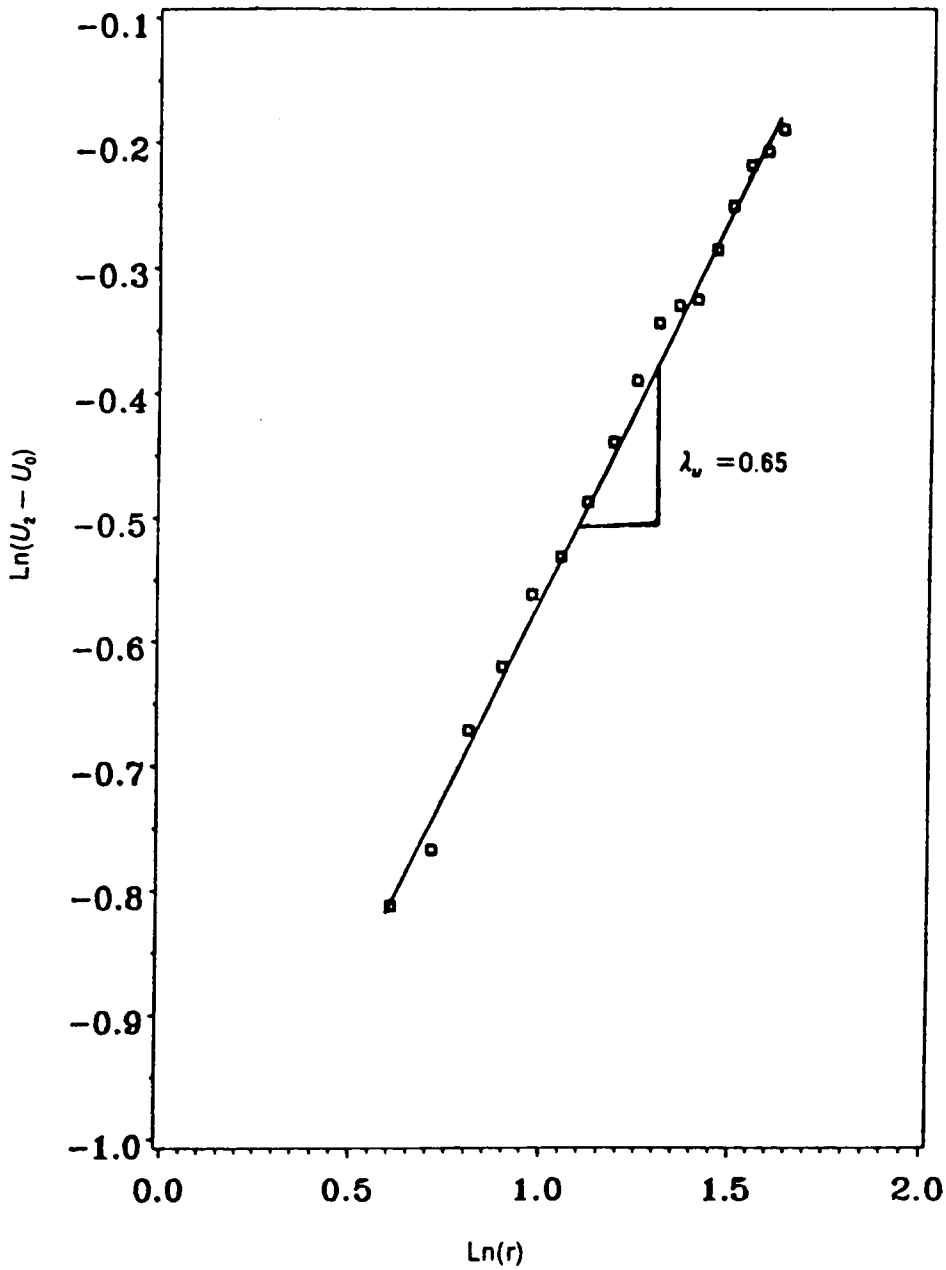

Figure 5.9. Displacement eigenvalue for inert propellant, slow rate.

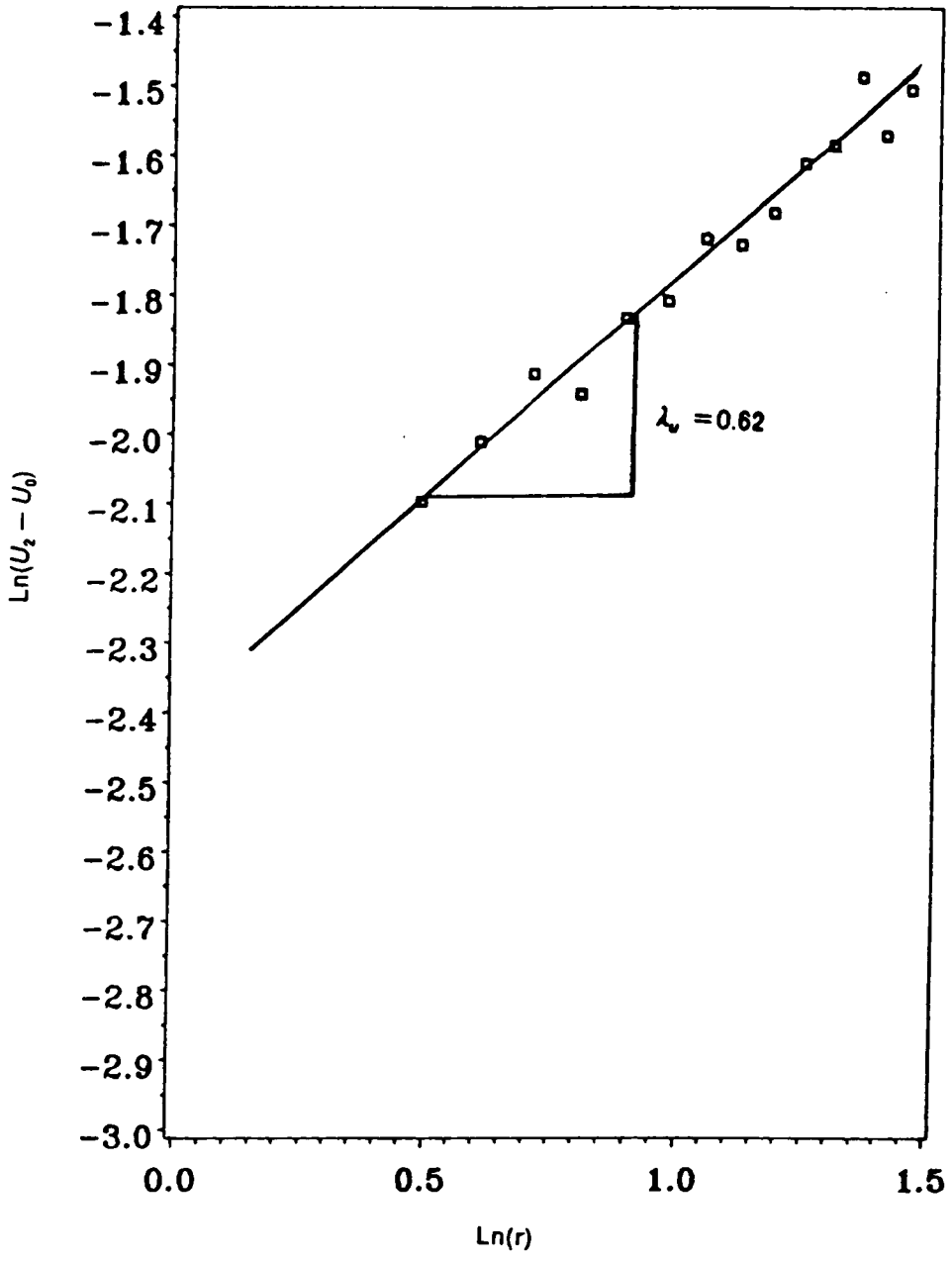

U_2, U_0 and r in millimeters

Figure 5.10. Displacement eigenvalue for inert propellant, fast rate.

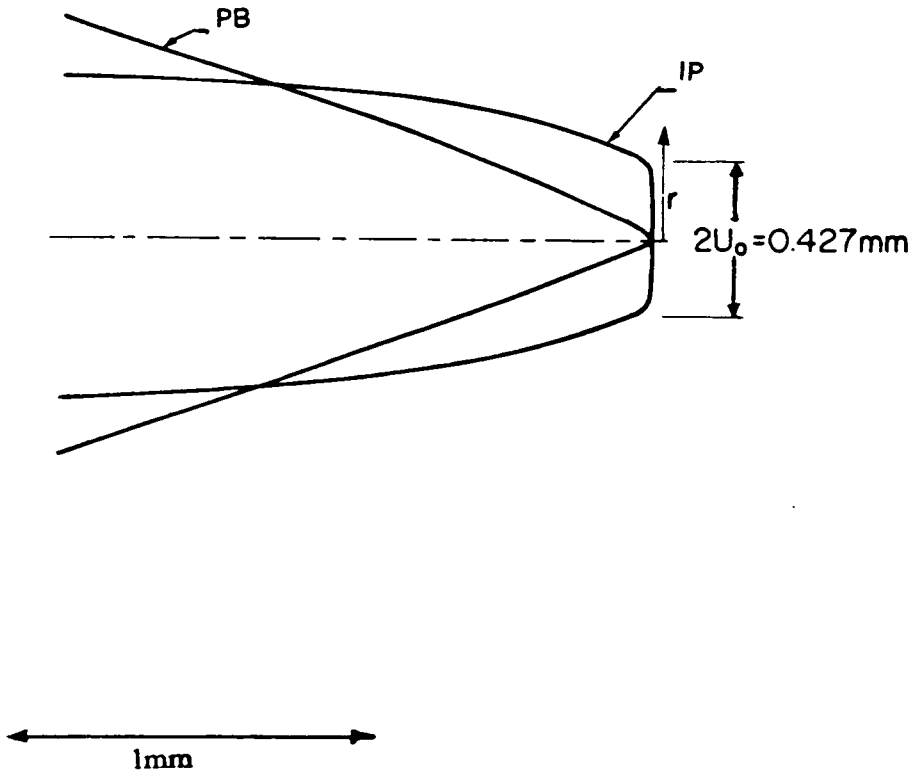

IP - Inert Propellant
PB - Pure Binder
ε_y = 3.2(%)
Head rate = 25.4 mm/min.

Figure 5.11. Crack shape for pure binder and inert propellant.

Table 5.3. The dominant eigenvalue for displacement for inert propellant tests.

Test 1			Test 2		
Linear Zone (range) = 3.5-5.0 mm Displacement Rate = 2.5 mm/min			Linear Zone (range) = 1.5-5.0 mm Displacement Rate = 2.5 mm/min		
ε%	λ_u	$2U_0$ (mm)	ε%	λ_u	$2U_0$ (mm)
1.5	.629	.102	.76	.642	0.
3.3	.744	.476	2.75	.674	.20
4.8	.532	.143	5.54	.582	.16
8.0	.648	.344	7.57	.652	.26
			10.81	.792	.13
			24.05	.712	0.
λ_u (avg) = .638			λ_u (avg) = .676		

Table 5.4. The dominant eigenvalue for displacement for inert propellant tests.

Test 3			Test 4		
Linear Zone (range) = 1.5-4.5 mm Displacement Rate = 25.4 mm/min			Linear Zone (range) = 1.5-5.0 mm Displacement Rate = 25.4 mm/min		
ε%	λ_u	$2U_0$ (mm)	ε%	λ_u	$2U_0$ (mm)
.79	.592	.044	1.67	.643	0.
1.58	.604	.136	5.64	.646	.18
3.16	.619	.384	6.43	.761	0.
6.43	.570	.247	8.03	.677	0.
10.38	.567	.186	13.64	.717	.08
12.74	.681	.144			
13.54	.741	.160			
λ_u (avg) = .625			λ_u (avg) = .689		

5.3 PSM-9 Results

The slices from stress freezing tests were photoelastically analyzed. The distance from the crack tip to the center of the fringes was recorded by application of the Tardy method and fringe multiplication unit.

The method of measuring τ_0 was covered in the chapter on algorithms and the reader is referred to Eqns. 4.17, 4.18, and 4.28. Figure 5.12 shows a plot for one slice past the boundary layer in which τ_0 was calculated using LEFM. This τ_0 was then used with Eqn. 4.31 to determine λ_σ. Figure 5.13 shows a plot for that region. Figure 5.14 shows a plot of λ_σ for the boundary layer zone, and Fig. 5.15 shows the determination of λ_σ at the free surface. Again, the free surface value is close to Benthem's and a measured value using moire. The value of τ_0 is approximately zero for the free surface.

A series of tests with artificial and natural cracks was run. The crack border was straight and thumbnailed, respectively. Any differences in the distributions of the singularity order for the straight and thumbnailed cracks were within the data scatter. The values of the stress singularity order, λ_σ, for these cases are plotted in Fig. 5.16. The values of the stress singularity order from Benthem's analysis [14,33] and the dominant eigenvalue for stress ($|\lambda_\sigma| = 1 - |\lambda_u|$) using moire [38] at the free surface are also shown.

5.4 Crack Blunting and Growth in Inert Propellant

As was mentioned earlier, inert propellant showed some blunting at the tip. It began during the crack opening and before the crack growth. This section tries to answer some of the

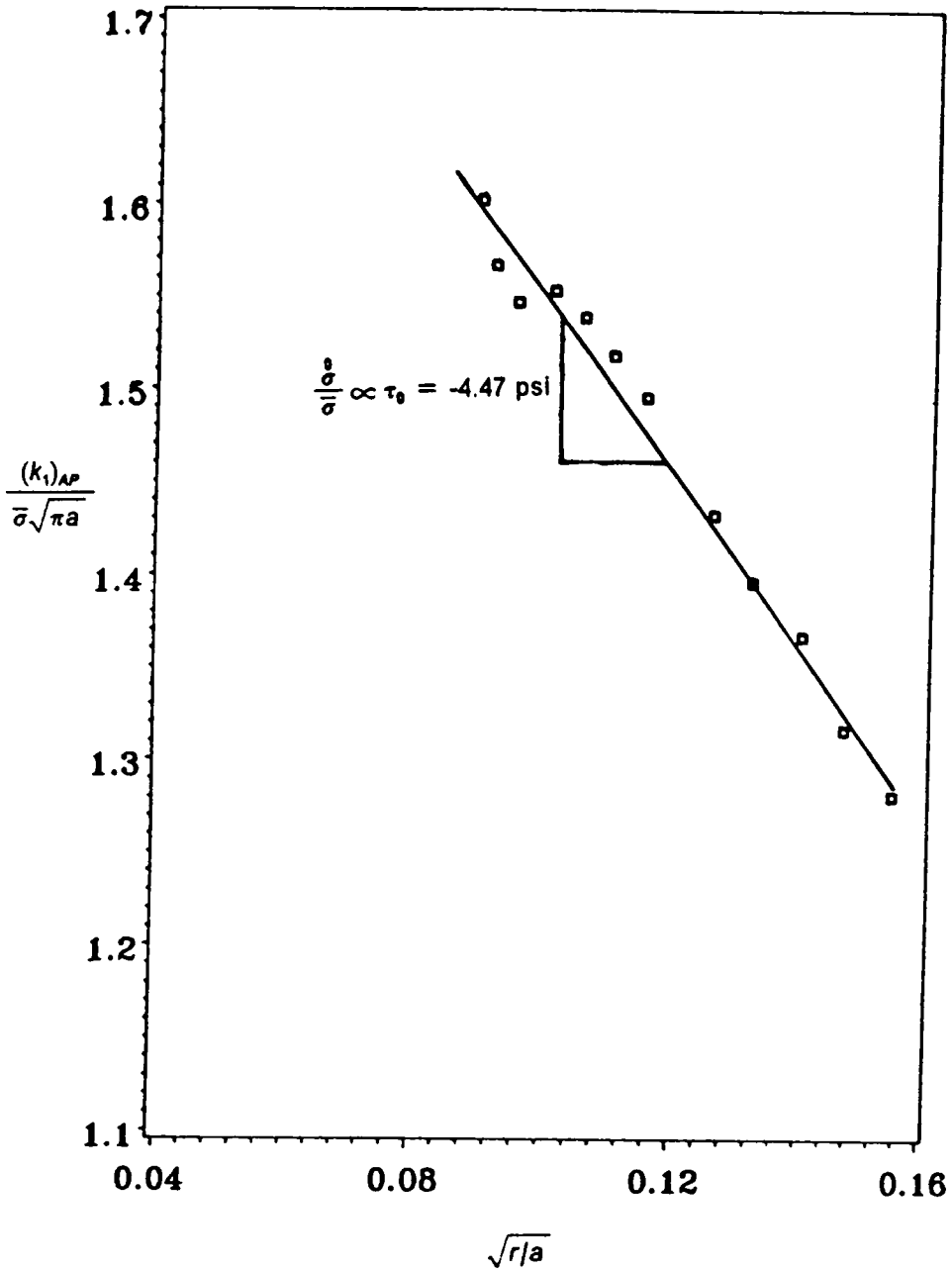

Figure 5.12. Measurement of the non-singular stresses for plain strain region.

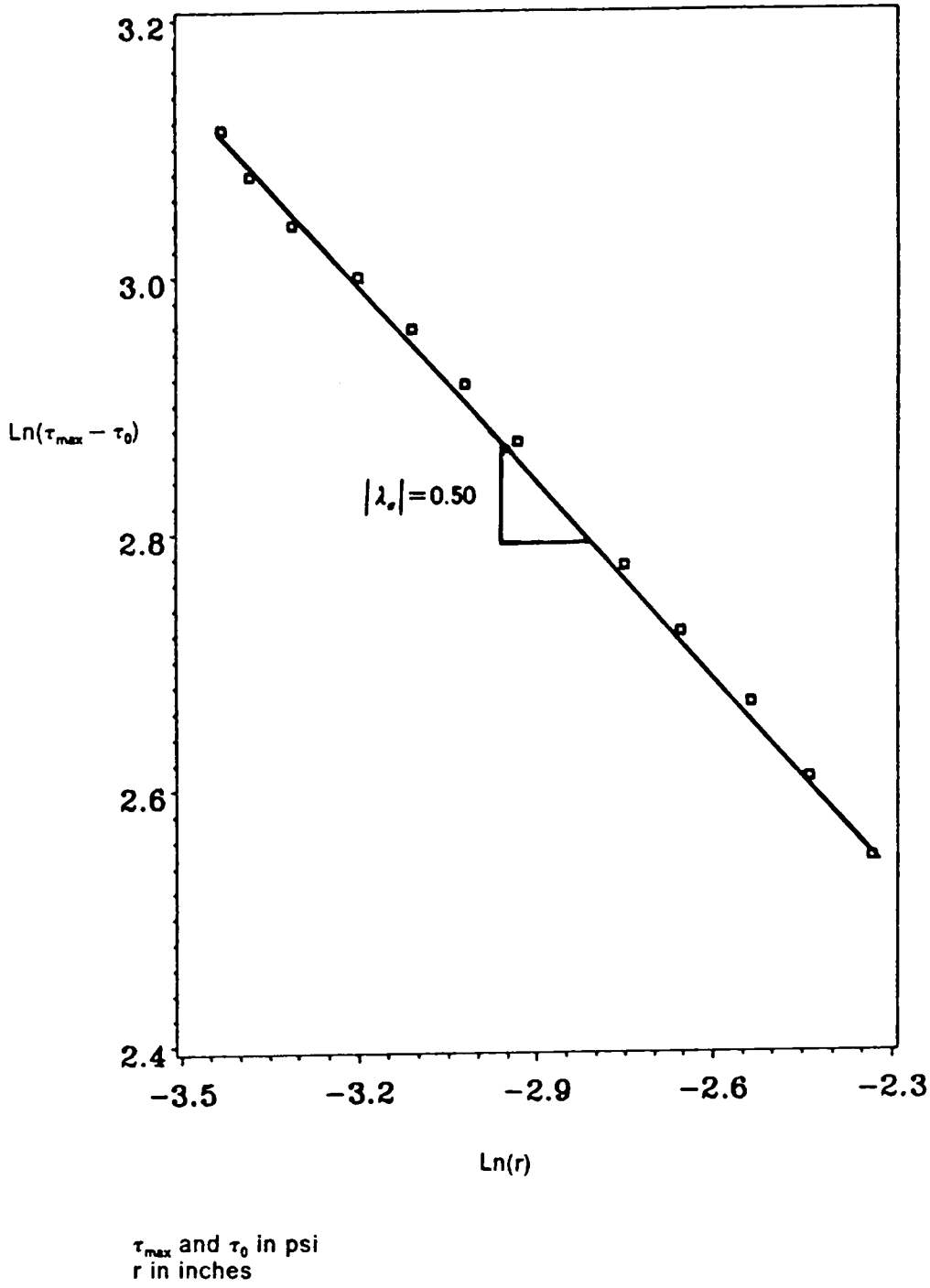

Figure 5.13. Plot of the stress singularity value of 1/2 for plane strain region.

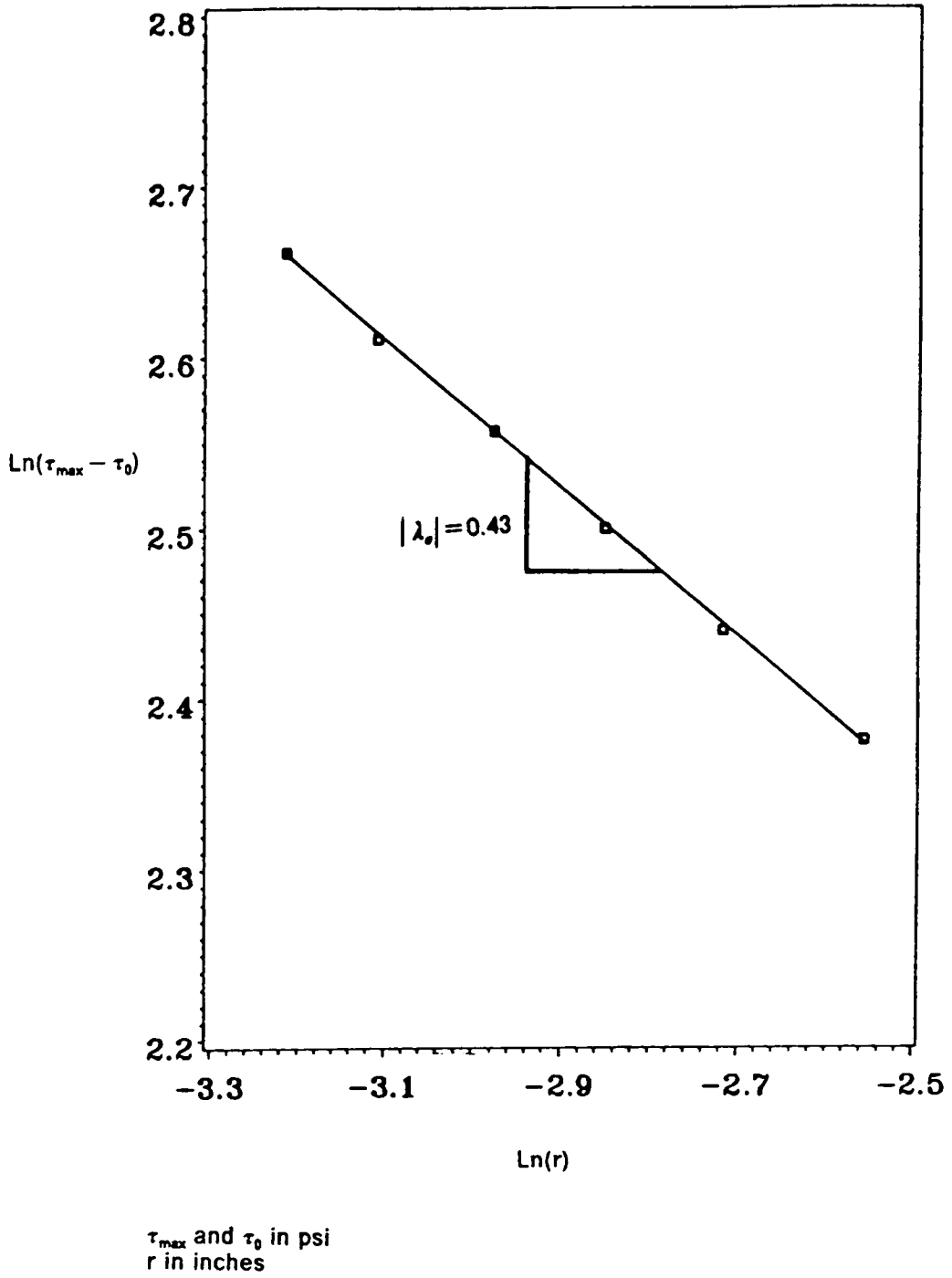

Figure 5.14. Plot of the stress singularity in the transition zone.

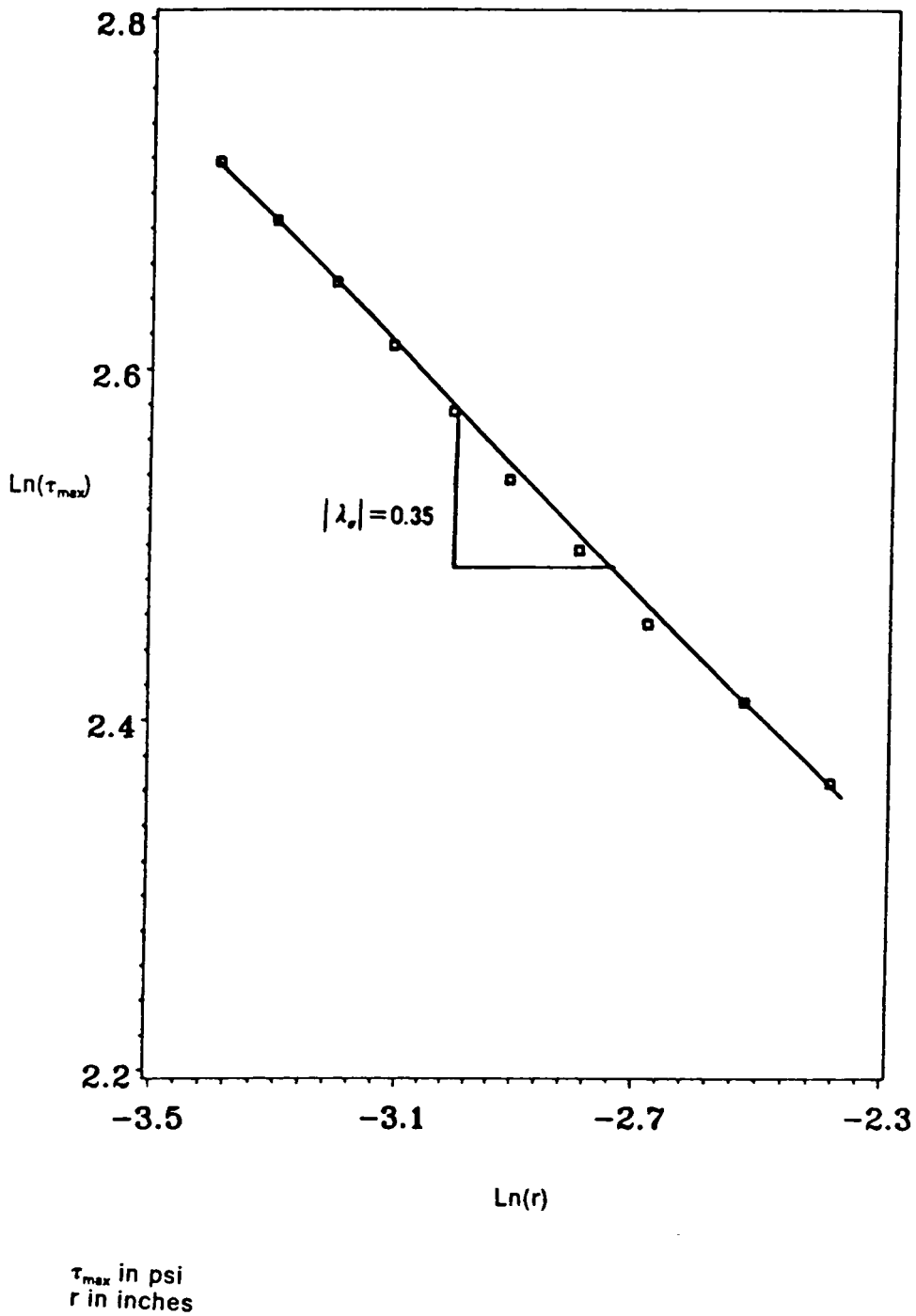

Figure 5.15. Plot of the stress singularity at the free surface.

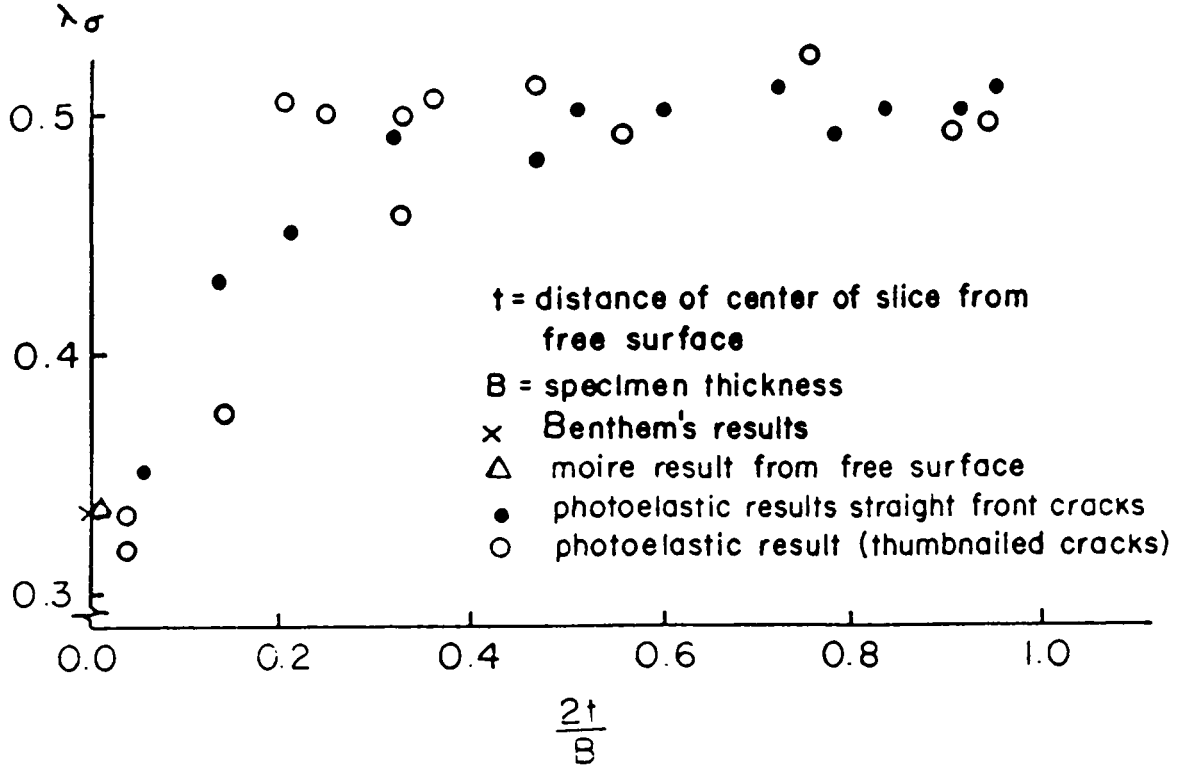

Figure 5.16. Stress singularity variation through thickness for stress freezing material.

questions that may arise regarding this process. It should be noted that the argument below is based on experimental observations during the tests with the knowledge of the nature of the inert propellant, i.e., the fact that crystals of different sizes are randomly dispersed in the matrix material. The cases explained below assume idealized orientations of crystals with respect to the crack plane as shown in their appropriate figures.

One case would be the alignment of the crystals in a perfect order along the lips of the crack, after it was inserted using a blade, as well as ahead of the crack tip. Figure 5.17 shows the crack with such an orientation of crystals. Figure 5.17a is after insertion of the crack, but before loading. As the load is applied in tension perpendicular to the crack plane, the crack would open up and then blunt. A blunted crack is shown in Fig. 5.17b. Upon loading, the rubber matrix along the crack plane extends as shown in the Fig. 5.17b. The extension is focused in this region, so the materials above and below the stretched zone carry a small portion of the stretching applied by the load.

Another orientation could be assumed to have crystals at an arbitrary angle of 45° with respect to the crack plane. Again the shape of the crack is the same as the matrix line ahead of the crack tip. Figure 5.18 has an illustration of this model. The behavior upon loading would be the stages of opening and blunting. The blunting would again be a triangular region ahead of the crack tip with its base as the blunt end. The matrix embedding the crystals adjacent to this zone, referred to as the pre-cracked zone, deforms little due to loading.

In theory, all the area between the crystals is filled with matrix material. But in reality there could be some air trapped at the interface of the crystals and matrix, or some locations where matrix and crystals have not bonded perfectly. If it happens that these 'imperfections' fall in regions ahead of the crack tip when the specimen is loaded and the pre-crack zone is formed, these imperfections would open up and could be observed as voids. Another explanation for the formation of the voids could be that the stretched matrix ahead of the crack can be regarded as tubes of rubber that are extended. Since these tubes are not strongly transversely

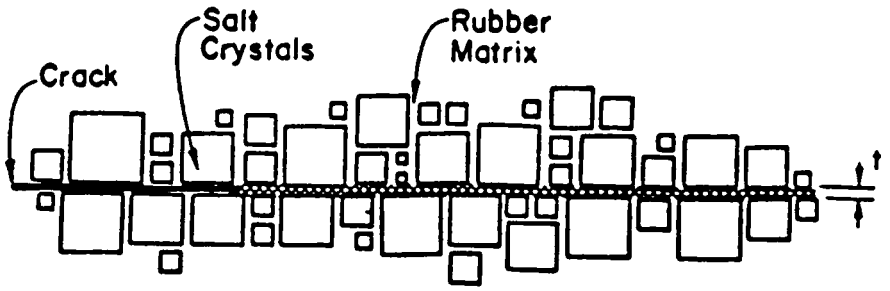

No load state

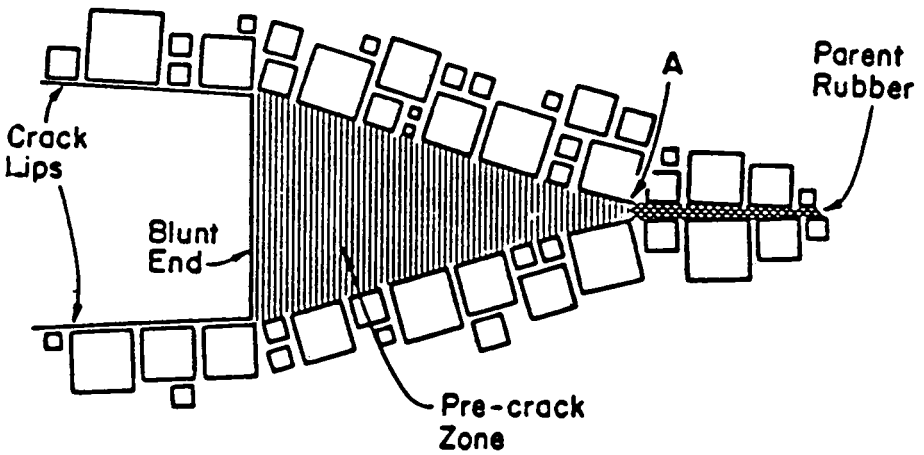

Loaded state with blunting shown at the crack tip

Figure 5.17. Crack location with idealized particles orientation in inert propellant [39].

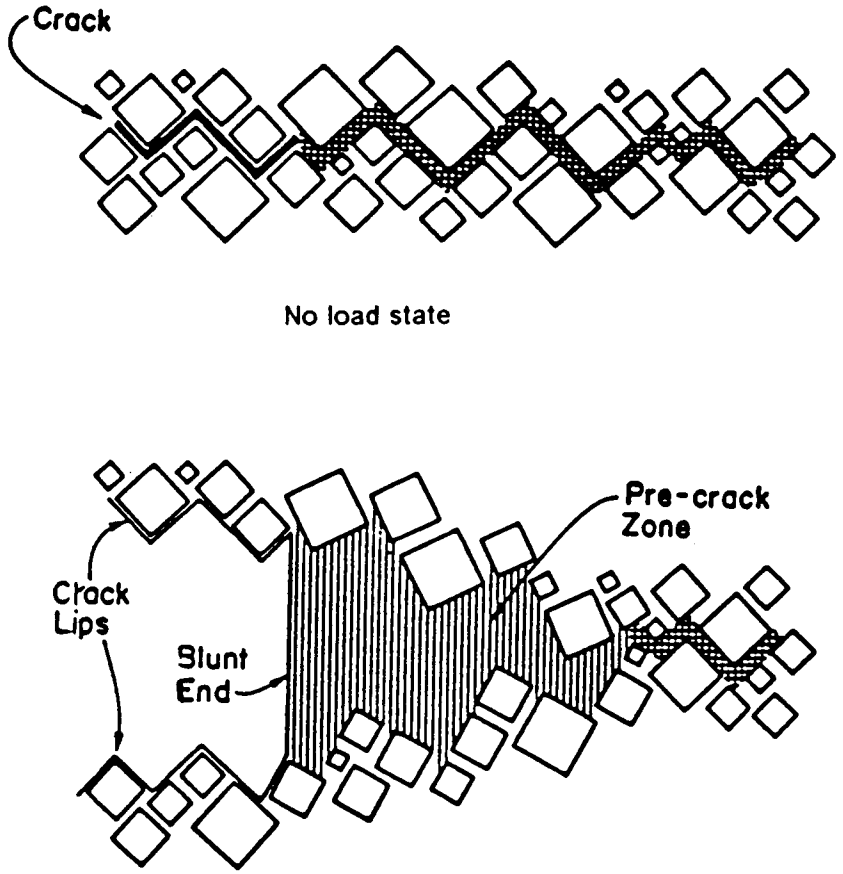

Figure 5.18. Crack location with idealized particles orientation in inert propellant [39].

connected, as the load increases they would fail and create voids. The voids get bigger and eventually the crack would run into voids that would result in extension of the crack, and this process continues up to failure of the specimen. Figure 5.19 shows the crack shape and the created voids ahead of the crack under load.

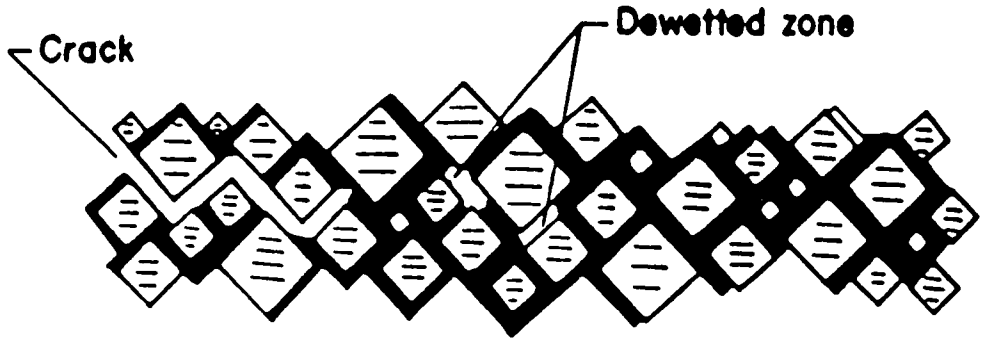

No load state

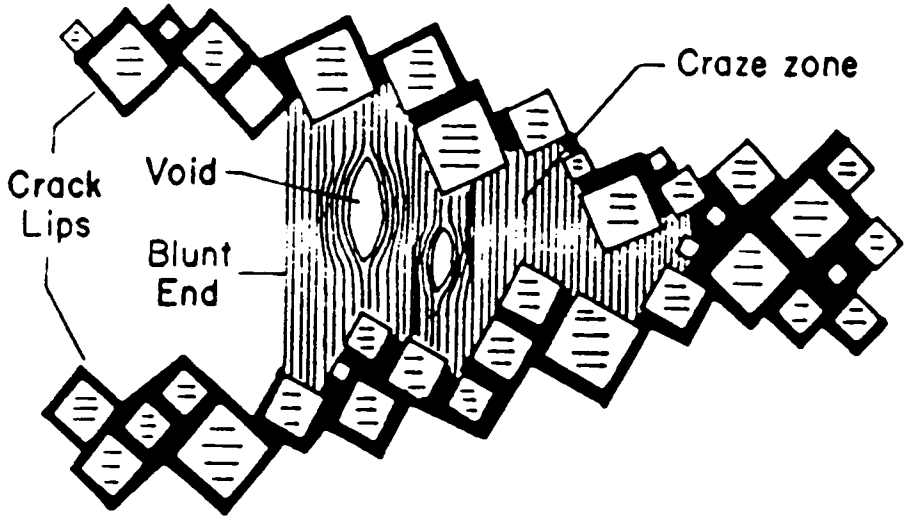

Loaded state with blunting shown at the crack tip

Figure 5.19. Creation of voids ahead of the crack tip in inert propellant [50].

6.0 Summary and Future Work

6.1 Summary

The behavior of inert propellant is not very well understood to date. Upon changing the percentage of its ingredients, the behavior changes as well. In this text, an investigation was experimentally directed towards a better understanding of this material with a crack in it. The dominant eigenvalue for displacement was calculated for inert propellant at the free surface. The distribution of the stress singularity through the thickness was conjectured to be similar to the three dimensional photoelastic material (PSM-9) and measured for the latter case. The values of the displacements and strains normal to the crack plane were also calculated and plotted for inert propellant.

The pure binder, the matrix material of the inert propellant, was also of interest and the same quantities were determined as for the inert propellant.

The crack front was photographed for inert propellant, pure binder, and PSM-9. There is no thumbnailing in the inert propellant specimens. This could be explained by the assumption

that resin-rich zone ahead of the crack is not strongly transversely connected. For pure binder, reverse thumbnailing was observed which was not expected. Since the material is soft, it could have been damaged in the process of inserting the initial crack and that would have caused the retardation of growth at the free surfaces. Additional tests should be performed for a better understanding of the crack border shape for the case of pure binder. The crack front for PSM-9 was thumbnailed in the case that it was naturally grown in the oven at the critical temperature. A series of tests were run on PSM-9 with an artificial straight front crack as well.

Severe blunting was observed in inert propellant at the crack tip. Upon loading, a resin rich region was created around and ahead of the crack tip. This region carries the high strains so the materials above and below it carry a small portion of the stretching applied by the load.

6.2 *Future Work*

This study would be considered complete in the sense that the variation of the dominant eigenvalue for stress was successfully measured and plotted against thickness. Engineers could take advantage of these values in their design codes, by using Finite Element programs that perform three dimensional analysis for materials.

The values of K_I could be calculated for these slices and plotted against thickness using the formulation and mapping functions developed by Smith [56].

The crack border for pure binder and inert propellant could be studied in more detail to see if the shape has any correlation with the stress singularity order or K_I. The effect of moisture on the test results could be investigated and taken into consideration as well.

After establishing a rich data base for this loading condition (pure tension), more complex loading systems could be adopted. The cracks that make an angle with the plane of the load (mixed mode analysis) could also be a good candidate for a better understanding of this material.

Higher loading rates seem to have potential in terms of crack growth behavior and the fracture parameters and should be investigated.

The final task could be in doing some numerical modeling which covers all the above mentioned criteria. If this model is generalized, it should predict the behavior of the new propellants that are fabricated without requiring extensive experimental work. One should always keep in mind that if the physics of the problem is understood correctly, experiments would be the best way to benchmark the developed theories.

References

1. Griffith, A.A., "The Phenomenon of Rupture and Flow in Solids," Phil. Trans., Royal Society of London, vol. 221, pp. 163-198, 1921.

2. Inglis, C.E., "Stresses in a Plate due to the Presence of Cracks and Sharp Corners." Trans. of the Inst. of Naval Architects, vol. 60, pp. 219, 1913.

3. Orowan, E., "Fatigue and Fracture of Metals," Proc. of the 1950 Conference at M.I.T., pp.139, 1950.

4. Irwin, G.R., "Fracture Dynamics Fracturing of Metals," Am. Soc. of Metals, Cleveland, pp. 147-166,1948.

5. Orowan, E., "Energy Criteria of Fracture," Welding Research Supplement, vol. 20, pp. 1575, 1955.

6. Irwin, G.R., "Onset of Fast Crack Propagation in High Strength Steel and Aluminum Alloys," VRL Dept., 4763 Proc. 1955 Sagamore Conference on Ordinance Materials, vol. 2, Syracuse, 1956.

7. Smith, C.W., "Fracture Mechanics," Chapter I, ESM 6050, ESM Dept., VA. Tech, Blacksburg, 1985.

8. Hartranft, R.J. and Sih, G.C., " The Use of Eigenfunction Expansions in the General Solution of the Three Dimensional Cracked Problems," J. of Math. and Mech., Vol. 19, No. 2, pp. 123-138, 1969.

9. Sih, G.C., "Three Dimensional Stress State in a Cracked Plate," Proc. of the Air Force Conf. on Fatigue and Fracture of Aircraft Structures and Materials, AFFDL TR 70-144.

10. Folias, E.S., "On the Three Dimensional Theory of Cracked Plates," J. of Appl. Mech., Trans. of ASME, pp. 663-674, 1975.

11. Folias, E.S., "Method of Solution of a Class of Three Dimensional Elastostatic Problems Under Mode I Loading," Int. J. of Fracture, vol. 16, pp. 335-348, 1980.

12. Benthem, J.P., "Three Dimensional State of Stress at the Vertex of a Quarter Infinite Crack in a Half-Space," Report WTHD No. 74, Delft Univ. of Technology, The Netherlands, 1975.

13. Benthem, J.P. and Koiter, W.T., (Discussion), Folias, E.S., (Closure), J. of Appl. Mech., Trans. of Asme, vol. 43, pp. 374-375, 1976.

14. Benthem, J.P., "The Quarter Infinite Crack in a Half-Space, Alternative and Additional Solutions," Int. J. of Solids and Structures, vol. 16, pp. 119-130, 1980.

15. Bazant, Z.P., "Three Dimensional Harmonic Function Near Termination or Intersection of Gradient Singularity Lines: A General Numerical Method," Int. J. of Engr. Science, vol. 12, pp. 221-243, 1974.

16. Bazant, Z.P. and Estenssoro, L.F., "Surface Singularity and Crack Propagation," Int. J. of Solids and Structures, vol. 15, pp. 405-426, 1979.

17. Swedlow, J. L., "Singularity Computations," Int. J. for Numerical Methods in Engr., vol. 12, pp. 1779-1798, 1978.

18. Takakuda, K., "Stress Singularities Near Crack Front Edges," Bull. JSME, vol. 28, pp. 225-231, 1985.

19. Smith, C.W., Epstein, J.S., and Olaosebikan, O., "Experimental Boundary Layer Studies in Three Dimensional Fracture Problems," Advances in Aerospace Structures, Mat'ls. and Dynamics, ASME-AO-06, pp. 119-126, 1983.

20. Smith, C.W., Olaosebikan, O., and Epstein, J.S., "A Proposed Rationale for Accounting for Boundary Layer Effects in Designing Against Fracture in Three Dimensional Problems," Proc. of XI Canadian Fracture Conf., pp. 209-220,1984.

21. Smith, C.W. and Epstein, J.S., "Experimental Boundary Layer Phenomena in High Poisson Ratio Fracture Mechanics," Proc. of U.S. Army Symposium on Solid Mech.," pp. 51-64, 1984.

22. Smith, C.W. and Epstein, J.S., "Measurement of Three Dimensional Effects in Cracked Bodies," Proc. of Vth Int'l. Congress on Expt'al Mechanics, Montreal pp. 102-110, 1984.

23. Smith, C.W. and Epstein, J.S., "Boundary Layer Measurements in Cracked Body Problems," SECTAM XII, pp. 355-360, 1984.

24. Smith, C.W., Lloyd, W.R., Rezvani, M., and Olaosebikan, O., " An Interpretation of Boundary Effects in Cracked Bodies," Proc. of Thirteenth Southeastern Conference on Theoretical & App. Mech., pp. 359-366, 1986.

25. Smith, C.W., Rezvani, M., and Lloyd, W.R., "Experimental Near Tip Methods of Analysis in Fracture Mechanics," Proc. of 1986 Conf. on Exp'tal. Mech. pp. 418-424, 1986.

26. Smith, C.W., Theiss, T.J., and Rezvani, M.,"Experimental Analysis of Crack Front Free Surface Intersection Phenomena," Proc. of 11th Canadian Congress of Appl. Mech., vol. 1, pp. A180-A181, 1987.

27. Smith, C.W., Rezvani, M., and Theiss, T.J., "Boundary Effects on Stress Singularities in Cracked Bodies," Proc. of 1987 Conf. of Soc. for Exp'tal Mech., pp. 215-220, 1987.

28. Smith, C.W. and Rezvani, M., "Measurement of Boundary Effects in Surface Flaws," Proc of Joint Int'l. Conf. of the British Society for Strain Measurement & the Society for Exp'tal Mech.,1987.

29. Smith, C.W., "On the Measurement of Some Three Dimensional Effects in Cracked Bodies," Proc. of 2nd Int'l Conf. on Comp. Engr. Sc., vol. 1, pp. 8, 1988.

30. Williams, M.L., "Stress Singularities Resulting from Various Boundary Conditions in Angular Corners of Plates Under Bending'" Proc. of the U.S. Nat'l. Congress of Appl. Mech., 1951.

31. Villarreal, G. and Sih, G., "Three Dimensional Photoelasticity: Stress Distribution Around a Through Thickness Crack," Exp'tal Evaluation of Stress Concentration and Intensity Factors, Mech. of Fracture, vol. 7, 1981.

32. Lloyd, W.R., "Experimental Determination of the Stress Singularity Exponent in Cracked Bodies Using Photoelasticity," Master's Thesis, VPI&SU. 1986.

33. Benthem, J.P., "On an Inversion Theorem for Conical Regions in Elasticity," J. of Elasticity, vol. 9, no. 2, 1979.

34. Benthem, J.P., "Graphs of the Three Dimensional State of Stress at the Vertex of a Quarter Infinite Crack in a Half-Space," Delft Univ., Report 123, 1980.

35. Kawai, T. and Fujitani, Y., "Analysis of a Singularity at the Root of the Surface Crack Problem," Proc. of the Int'l. Conf. on Fracture Mech., pp. 1157-1163, 1977.

36. Kawai, T. and Fujitani, Y., "Analysis of Three Dimensional Surface Crack Problems by Boundary Integral Method," Seisan-Kenkyu, vol. 1, no. 2., pp. 26-29, 1976.

37. Burton, W.S. and Swedlow, J.L., et al., "On the Implications for Finite Element Method on the Three Dimensional Aspects in Some Crack/Surface Intersection Problems," Int'l. J. of Fracture, vol. 25, pp.3-32, 1984.

38. Epstein, J.S., "On the Variation of the First Classical Eigenvalue of Fracture Mechanics in the Three Dimensional Transitory Stress Field," Ph.D. Dissertation, VPI & SU, 1983.

39. Post, D., Smith, C.W., and Czarnek, R., "Crack Opening and Extension in Inert Solid Propellant, An Experimental Study," Final Report to Air Force Astronautics Laboratory for the Period 30 Sept., 1985 to 31 March, 1987.

40. Photoelastic Division, "Bulletin S-116-B," Measurement Group, Inc., Raleigh, N.C..

41. Parks, V.J., "Strain Measurements Using Grids," Society of Photo-Optical Instrumentation Engrs., vol. 21, no. 4, pp. 633-639, 1982.

42. Czarnek, R., Post, D., and Lee, J., "Experimental Analysis of the Fracture Process of Simulated Solid Rocket Propellant," Proc. of the VI Int. Congress on Experimental Mechanics, Portland, Oregon, June 1988.

43. Smith, C.W., "Use of Three Dimensional Photoelasticity and Progress in Related Areas," Ch.1 of Experimental Techniques in Fracture Mechanics, SESA monograph; no. 2. pp.3-58, 1975.

44. Tardy, M.H.L., "Methode Pratique d'examen de mesure dela birefringence des verres d'optique," Rev. Opt., vol. 8, 1929.

45. Dally, J.W. and Riley, W.F., "Experimental Stress Analysis," Ch. 13, McGraw Hill Book Company, Second Edition, 1978.

46. Epstein, J.S., Post, D., and Smith, C.W., "Three-Dimensional Photoelastic Measurements with Very Thin Slices," Experimental Techniques, pp. 34-37, Dec. 1984.

47. Post, D., "Fringe Multiplication in Three Dimensional Photoelasticity," J. of Strain Analysis, vol. 1, no. 5, pp. 380-388, 1966.

48. Post, D., "Isochromatic Fringe Sharpening and Fringe Multiplication in Photoelasticity," Proc. Soc. Expt'al. Stress Analysis, vol. 12, no. 2, pp. 143, 1955.

49. Theiss, T.J., "Preliminary Investigation into the Cracking of Polyurethane," Master's Thesis, VPI & SU, 1987.

50. Post, D., Smith, C.W., and Czarnek, R., "Boundary Layer and Singularity Measurement in Three Dimensional Fracture Problems," Final Report to Air Force Astronautics Laboratory for the Period Aug. 1987 to Aug. 1988.

51. Eftis, J., Subramonian, N., and Liebowitz, H., "Crack Border Stress and Displacement Equations Revisited," J. of Engineering Fracture Mechanics, vol. 19, no. 1, 1977.

52. Kassir, M. and Sih, G.C., "Three Dimensional Stress Distribution Around an Elliptical Crack Under Arbitrary Loading," J. of Appl. Mech., ASME Trans., Sept. 1966.

53. Smith, C.W., Czarnek, R., and Rezvani, M., "Determination of Continuum Fracture Parameters for a Particulate Composite," Recent Advances in Micro-Macro Mechanics of Composite Materials, ASME Winter Annual Mtg., Chicago, IL., Nov. 1988.

54. Smith, C.W., Chang, C.W., and Rezvani, M., "Analysis of Optical Measurements of Free Surface Effects on Natural Surface and Through Cracks," Symposium on Surface Crack Growth, Reno, Nevada, April 1988.

55. Nadai, A., "Uber die Spannungsurefeilung in einer durch eine Einzelkraft belasteten rechtekigen Platte," Der Bauingeneiur, vol. 2, pp. 11-16, 1921.

56. Smith, C.W., Lloyd, W.R., and Olaosebikan, O., "An Interpretation of Boundary Effects in Cracked Bodies," Proc. of 13th Southeastern Conference on Theoretical and Applied Mechanics," April 1986.

The vita has been removed from the scanned document